

## Recent mantle degassing recorded by carbonic spring deposits along sinistral strike-slip faults, south-central Australia



Uwe Ring <sup>a,\*</sup>, I. Tonguç Uysal <sup>b,c</sup>, Galip Yüce <sup>c</sup>, Ezgi Ünal-İmer <sup>b,d</sup>, Francesco Italiano <sup>e</sup>, Ali İmer <sup>f</sup>, Jian-xin Zhao <sup>g</sup>

<sup>a</sup> Department of Geological Sciences, Stockholm University, 10691 Stockholm, Sweden

<sup>b</sup> Queensland Geothermal Energy Centre of Excellence, The University of Queensland, QLD 4072, Australia

<sup>c</sup> Department of Geological Engineering, Hacettepe University, Ankara 06800, Turkey

<sup>d</sup> School of Geography, Planning & Environmental Management, The University of Queensland, QLD 4072, Australia

<sup>e</sup> Istituto Nazionale di Geofisica e Vulcanologia, sezione di Palermo, Italy

<sup>f</sup> Department of Geological Engineering, Middle East Technical University, Ankara 06800, Turkey

<sup>g</sup> School of Earth Sciences, The University of Queensland, QLD 4072, Australia

### ARTICLE INFO

#### Article history:

Received 18 April 2016

Received in revised form 16 July 2016

Accepted 9 September 2016

Available online 4 October 2016

Editor: A. Yin

**Keywords:**  
neotectonics  
lithospheric structure  
strike-slip fault  
structural geology  
geochemistry  
Australia

### ABSTRACT

The interior of the Australian continent shows evidence for late Quaternary to Recent fault-controlled mantle  $^3\text{He}$  and  $\text{CO}_2$  degassing. A series of interconnected NW-striking sinistral faults, the Norwest fault zone (NFZ), in south-central Australia are associated with travertine mounds, the latter show a regular spacing of 50–70 km. U-series ages on 26 samples range from  $354 \pm 7$  to  $1.19 \pm 0.02$  ka ( $2\sigma$  errors) and suggest a clustering every  $\sim 3$ –4 ka since  $\sim 26$  ka. Geochemical data demonstrate a remarkable mantle-to-groundwater connection. Isotopic data indicate that the groundwater is circulating to depths  $>3$  km and interacting with Neoproterozoic/Cambrian basement and mantle volatiles.  $^3\text{He}/^4\text{He}$  isotope ratios show that the He comes in part from the mantle. This demonstrates that the NFZ cuts through the entire crust and provides pathways for mantle degassing. Scaling relationships suggest that the series of sinistral faults that make up the NFZ are interconnected at depths and have a significant strike length of 60–70 km or more. The NFZ occurs where a major compositional boundary and a significant heat flow anomaly occurs, and a major step in lithospheric thickness has been mapped. We discuss a tectonic model in which recent stress field, heat flow and lithospheric structure in central Australia reactivated a set of steeply dipping Neoproterozoic faults, which may now be growing into a crustal/lithospheric-scale structure.

© 2016 Elsevier B.V. All rights reserved.

### 1. Introduction

Australia is the lowest and flattest of all continents, which is consistent with a stable, cratonic lithosphere far away from any plate boundary (Sandiford and Quigley, 2009) (Fig. 1). Yet, Australia is among the most active 'stable continental regions' (Braun et al., 2009). Some Australian sedimentary basins have substantially large  $\text{CO}_2$  outgassing (Boreham et al., 2001), which is associated with mantle-derived He in parts of the Great Artesian Basin (Torgersen and Clarke, 1985), a phenomenon characteristic of seismically active zones (Kennedy et al., 1997). There are indeed zones of active seismicity in the interior of the Australian continent causing earthquakes with magnitudes of up to 7 (Hillis et al., 2008) (Fig. 2).

Furthermore, numerous faults with Miocene to Quaternary displacements have been documented (Waclawik et al., 2008).

Another indicator of neotectonic activity in south-central Australia is the widespread occurrence of carbonic springs and travertine deposits along faults extending from the basement to the surface (Adlam and Kuang, 1988). Gold and Soter (1984) have noticed a correlation between major  $\text{CO}_2$  seeps and zones of enhanced seismicity, and suggested that mantle or metamorphic  $\text{CO}_2$  ascending through the crust along active faults triggers earthquakes. In the Flinders Ranges in south-central Australia, Balfour et al. (2015) showed that deeply sourced crustal fluids are associated with active faulting and that the focused seismicity there can only be explained by high pore-fluid pressure in the lower crust. Most faults associated with carbonic springs in south-central Australia strike NW–SE. Near Lake Eyre, calcite vein networks are prominent and occur in fracture zones associated with a neotectonic fault array, the Norwest fault zone (NFZ; Geological Survey of South Australia, 1992) (Fig. 2). Travertine deposits in seismically active

\* Corresponding author.

E-mail address: [uwe.ring@geo.su.se](mailto:uwe.ring@geo.su.se) (U. Ring).

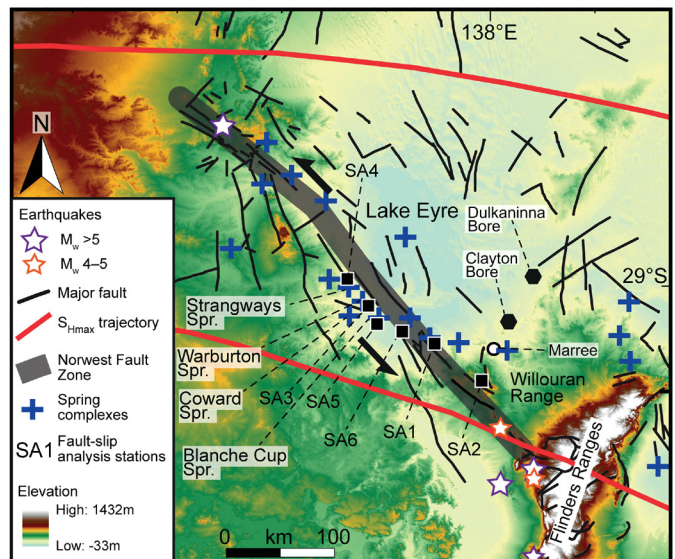
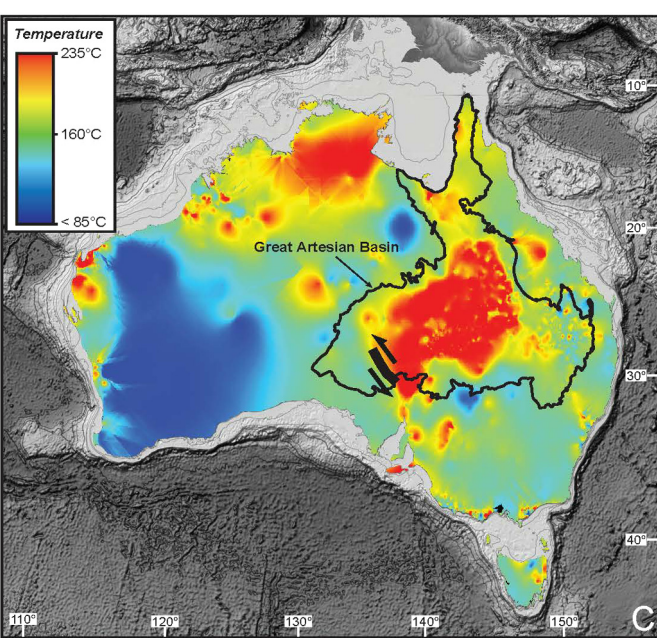
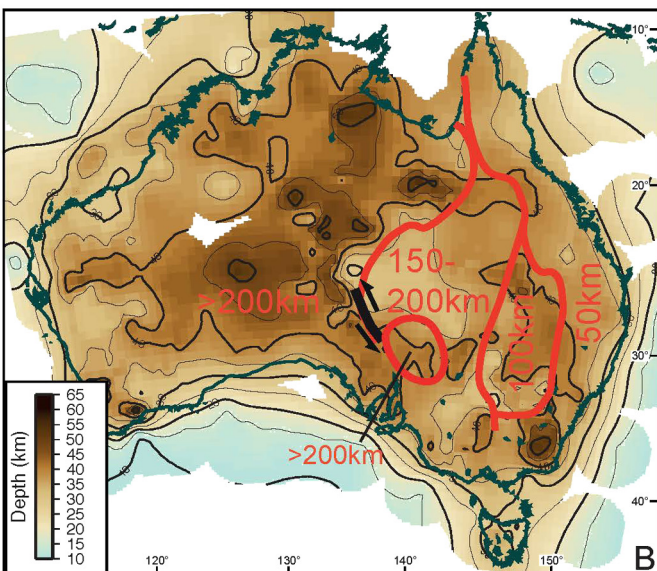
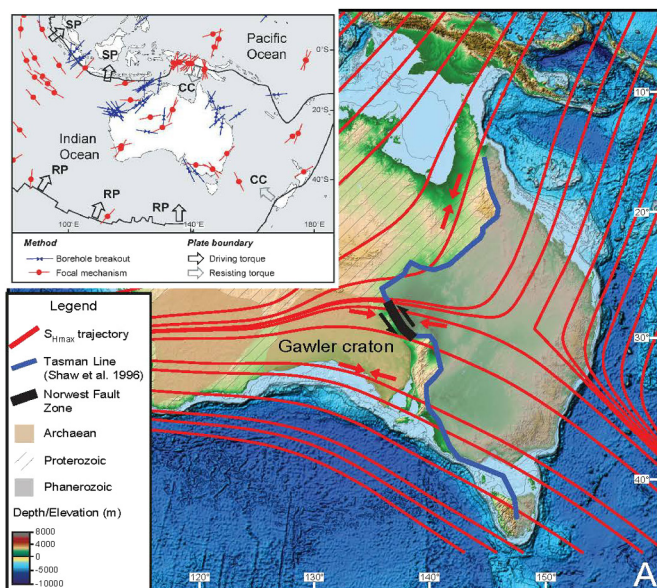


**Fig. 2.** Topographic map of northern south-central Australia showing NFZ near Marree,  $S_{Hmax}$  trajectories, carbonic spring complexes straddling NFZ at spacing of some 50–70 km, major earthquakes and localities for fault-slip analysis (SA1 through SA6); note uplift of N–S-trending Flinders Range subperpendicular to  $S_{Hmax}$  trajectories, subdued topography around NFZ and Lake Eyre basin. Base map from Geoscience Australia, national elevation data framework portal (<http://nedf.ga.gov.au/geoportal/catalog/main/home.page>); earthquake data from South Australian Government (South Australian Resources Information Geoserver, SARIG, <https://sarig.pir.sa.gov.au/MapViewerJS>).

zones provide an important record of fault movement, as they can be dated precisely using U-series methods (Uysal et al., 2011; Kampman et al., 2012).

Although active tectonics has been known as the main process for transferring mantle volatiles into shallow crustal environments (Kulogoski et al., 2005; Kennedy and van Soest, 2007), a possible connection between recent fault movements and mantle degassing in Australia remained largely enigmatic. We show that the NFZ contains surface vents allowing mantle degassing in the Australian craton by examining the structure, geochronology, and isotope geochemistry of fault-controlled travertine deposits and dissolved and free gas samples. Specifically, we provide a solid data set on the exact timing of episodic  $^3\text{He}$  and  $\text{CO}_2$  degassing events and related late Quaternary to Recent fault activity.

## 2. Setting

Australia is the fastest moving continent since the Eocene (Sandiford et al., 2004) and has migrated more than 3000 km to the NNE as part of the Indo-Australian Plate (DeMets et al., 2010). Fast motion of Australia is controlled by the slab-pull force related

**Fig. 1.** (A) Topographic map of Australia (<http://maps.ngdc.noaa.gov>) with orientation of modeled maximum horizontal stress trajectories ( $S_{Hmax}$ , Hillis and Reynolds, 2000; Dyksterhuis and Müller, 2008); southern part of Australia characterized by E–W  $S_{Hmax}$  that swings into NNE direction subparallel to plate velocity vector in north; also shown are main crustal provinces, outlines of major cratons and Tasman Line proposed by Shaw et al. (1996) using geophysical signatures and locations of surface outcrop to define boundary. Inset: Indo-Australian Plate with in-situ stress data showing  $S_{Hmax}$  and plate boundary forces (RP: ridge push, SP: slab pull; CC: continental collision) (Sandiford et al., 2004). (B) Crustal thickness map (Kennett et al., 2011), note relatively thin crust in south-central Australia broadly coinciding with topographic low of Lake Eyre basin with altitude below sea level; lithospheric thicknesses also shown (Fishwick et al., 2008). (C) Heat flow map of Australia showing modeled crustal temperature at five kilometers depth ([www.ga.gov.au](http://www.ga.gov.au)). Surface trace of NFZ indicated on all maps; note that fault zone coincides with step in lithospheric thickness, relatively thin crust, transition from low to high heat flow in south-central Australia, and broadly also with swing in  $S_{Hmax}$  direction from E–W to NNE.

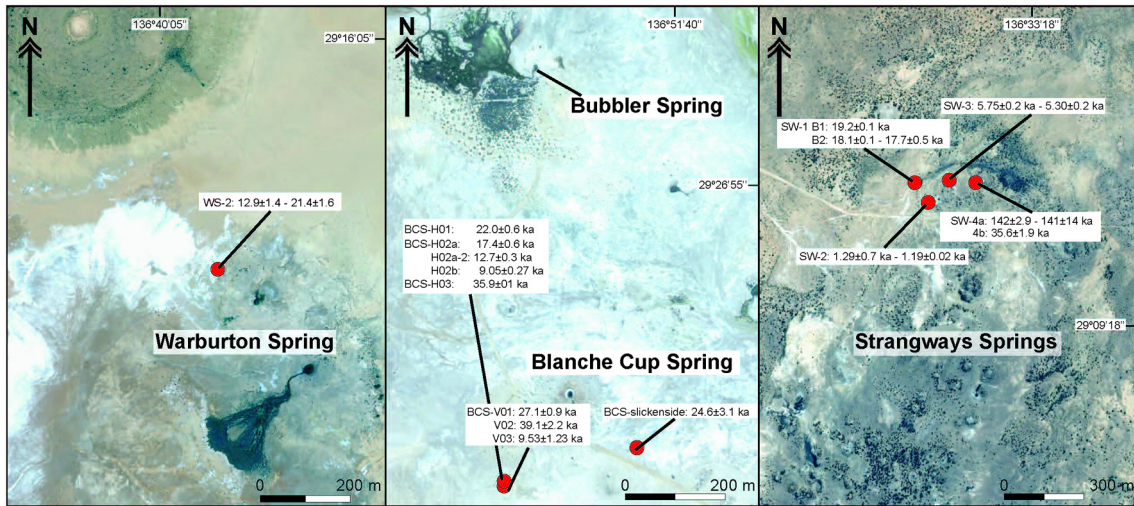


**Fig. 3.** Satellite images of carbonate spring complexes (data source: [www.esri.com](http://www.esri.com)) showing sample localities with U-series ages listed in Table 1 (note that age range for WS-2, SW-1 B2, SW-2, SW-3, SW-4 given). Refer to Fig. 2 for location of the spring complexes.

to subduction in Indonesia and is resisted by continent collision in the Himalayan, Southern Alps and New Guinea orogens (Sandiford and Quigley, 2009) (Fig. 1). The forces associated with this plate-tectonic configuration caused high asthenospheric shear beneath Australia (Conrad et al., 2011) and shaped the intra-plate in-situ stress field (Dyksterhuis and Müller, 2008) (Fig. 1A).

An important tectonic feature of central Australia is that the cratonic blocks of western Australia border the Neoproterozoic/Phanerozoic orogens of east Australia (Fig. 1A). This boundary straddles the Tasman Line across which changes in crustal thickness and composition occur (Shaw et al., 1996). In addition, Fishwick et al. (2008) showed a major step in lithospheric thickness from >200 km in the west to ~150–200 km in the east along a NW-striking zone in the vicinity where Shaw et al. (1996) proposed the Tasman Line (Fig. 1B). There is also an important change in heat flow near this boundary (Neumann et al., 2000) (Fig. 1C).

Célérier et al. (2005) and Holford et al. (2011) noted that there is a spatial correspondence of regions of high heat flow and neotectonic structures and/or seismicity. The striking difference in heat flow across the boundary in south-central Australia shown in Fig. 1C resulted from burial of basement enriched in heat producing elements and implies that Moho temperatures could be ~90–120 °C hotter to the east, sufficiently high to reduce bulk lithosphere strength by a factor of 2–5 and focus deformation (Célérier et al., 2005). Therefore, the latter authors attributed active intra-plate deformation in south-central Australia to thermal weakening. However, numerical modeling by Dyksterhuis and Müller (2008) shows that rheological contrasts between geological provinces and evolving plate boundary forces could explain strain localization. Yet another proposition by Balfour et al. (2015) claims that intra-plate faulting is caused by high pore-fluid pressure.

The Lake Eyre region of south-central Australia is characterized by numerous NW-striking, subvertical faults (Fig. 2), which are associated with carbonic spring complexes and are seismically active. The NW-striking faults reactivate Neoproterozoic and Mesozoic/Cenozoic structures (Adlam and Kuang, 1988). For this study, travertine samples were collected from carbonic spring complexes that decorate the NW-striking Norwest Fault zone (NFZ, Figs. 2, 3). The NFZ occupies a critical position with regard to crustal/lithosphere thickness, crustal province boundaries and change in stress directions in south-central Australia (Fig. 1). The NFZ straddles the boundary between the Gawler craton in the west and the Cambrian Delamerian orogen (Flinders Ranges) in the east, thus fringing the Precambrian cratonic margin of south-central Aus-

tralia (Paul et al., 1999). The NFZ probably formed by 800 Ma as a normal fault controlling Neoproterozoic/Cambrian sedimentation in the Adelaide geosyncline (Jenkins, 1990) and was reactivated during the Delamerian orogeny (Paul et al., 1999). The Neoproterozoic/Cambrian basement rocks (basement in the remainder of the paper) are overlain by a series of superimposed Mesozoic to Recent intra-cratonic sedimentary basins, including the Jurassic/Cretaceous Eromanga and the Cenozoic Lake Eyre basins. The basin sediments have a cumulative thickness of ~3 km above basement and were deformed by reactivation of the NFZ (Adlam and Kuang, 1988). As such, the NFZ represents a major, long-lived, repeatedly reactivated fault.

### 3. Methods and analytical procedures

#### 3.1. Fault-slip analysis

The fault zones associated with the carbonic spring deposits are characterized by up to 15 m wide zones of intense cataclasis and fault gouge, the latter of which is usually up to a few decimeters thick. The fault planes are best developed in basement rocks (Fig. 4a) and contain frictional-wear striae. We have also collected fault-slip data in Eromanga Basin sediments and carbonic spring deposits (Fig. 4b). On the Curdimurka geologic map (Geological Survey of South Australia, 1992), the young faults controlling the travertine deposits continue along strike into Eromanga Basin sediments and basement. It is along those faults where we collected fault-slip data in basement and Eromanga sediments. In the vicinity of the main fault planes, arrays of minor striated faults coated with millimeter- to centimeter-thick fault gouge occur and the fault-slip data were collected on those minor faults. The main argument for relating the minor faults to the kinematic evolution of the NFZ is their spatial relationship to the major faults that make up the NFZ.

To evaluate the kinematics of the faults, the orientation of primary and secondary fault and foliation planes, plunging directions of striations and the sense of relative displacement on these planes were mapped for determining principal strain axes (Marrett and Allmendinger, 1990). Fiber orientations on slickensides are usually simple, consistent, and are readily interpretable with the geometry of the studied fault zones at the regional scale. The displacement of the measured minor fault planes was generally in the centimeter to decimeter range. A simple method has been used to determine principal strain axes from these crosscutting faults

and associated slickensides (program 'Fault Kinematics' written by R. Allmendinger). For distinguishing between the shortening and extension axes, the relative sense of slip is needed, which can be deduced from the orientation of fibers and Riedel planes associated with the fault (Petit, 1987).

Marrett and Allmendinger (1990) proposed that the brittle deformation in a faulted region can be directly related to the geomet-

ric moment, which may be expressed as the product of the average displacement and the fault surface area. This approach requires weighting the fault-slip data with the displacement and the fault surface area. Once the moment tensors are summed, strain magnitudes can be calculated. However, we have no information about slip magnitudes and fault surface area. Therefore, we can only determine the orientations (eigenvectors) of the principal strain axes. The absolute magnitudes (eigenvalues) cannot be calculated. The eigenvalues reported in Supplementary Table S1 are normalized and a proxy of the strain symmetry (see Ring, 2008 and Ring and Gerdes, 2016, for fuller description). Bingham distribution statistics for axial data are used to optimize clusters of kinematic axes of a fault array (Mardia, 1972). The linked Bingham distribution is equivalent to an unweighted moment tensor summation (a moment tensor sum in which all faults are weighted equally).

### 3.2. Gas analyses

The collected gas sample suite is composed of free and dissolved gas samples. The water samples (Fig. 4c, d) were stored in 240 ml pyrex bottles sealed in the field using silicon/teflon septa and purpose-built pliers (Italiano et al., 2009). The laboratory procedures for both free and dissolved gas were identical. The gas was extracted after equilibrium was reached at constant temperature with a high-purity argon gas phase injected into the sample bottle (Italiano et al., 2014). The composition of the dissolved gas phase was calculated using the solubility coefficients of each gas species, the volume of the extracted gas, and the volume of the extracted water sample (Italiano et al., 2009, 2014). Chemical analyses were carried out by gas chromatography (Perkin Elmer Clarus 500 equipped with a double TCD-FID detector) using argon as the carrier gas. Typical uncertainties were within  $\pm 5\%$ .

Helium isotope analyses were done on extracted gas fractions following Hilton (1996). Isotopic analyses of the purified helium fraction were performed using a static vacuum mass spectrometer (GVI 5400 TFT) that allows the simultaneous detection of  ${}^3\text{He}$  and  ${}^4\text{He}$  ion beams, thereby keeping the  ${}^3\text{He}/{}^4\text{He}$  measurement errors low. Typical uncertainties of samples with low  ${}^3\text{He}$  content are  $\pm 2\%$ .

The isotopic composition of the total dissolved carbon (TDC),  $\delta^{13}\text{C}_{\text{TDC}}$ , of the water samples was measured on 2 ml of water sample introduced in containers where high purity helium was



**Fig. 4.** Photos of fault planes, springs and dated samples from NFZ. (a) Fault surface with moderately plunging striations and breccia developed in silicified Neoproterozoic/Cambrian basement rocks west of Marree. (b) Dated calcite striations on fault surface, sample BCS-slickenside, Blanche Cup Spring. (c) Bubbler Spring sampling site for He-isotope studies. (d) Recent travertine deposited directly from  $\text{CO}_2$ -rich Great Artesian Basin water artificially released from bore. (e) Calcite vein in Jurassic/Cretaceous sediment in Willouran Range with U-series age, note two phases of vein-filling calcite. (f–m) Sample photos providing details of dated travertine samples from spring deposits; Warburton Spring (WS), Strangways Spring (SW), Blanche Cup Spring (BCS); individual veins separated by sharp contacts; U-series dating spots displayed with age results (Table 1). (f) Sample WS-2 with rhythmic bands providing ages of  $21.4 \pm 1.6$ ,  $12.9 \pm 1.4$  and  $12.4 \pm 1.1$  ka (note that the latter two ages are analytically indistinguishable) indicating distinct growth hiatus between  $\sim 21$  and  $\sim 12$  ka. (g) Sample SW-1 with U-series dating spots indicating growth hiatus between  $19.2 \pm 0.1$  ka and  $18.1 \pm 0.7/17.7 \pm 0.5$  ka; individual veins have sharp contacts marked by brown-yellow-black material providing evidence of vein growth during periodic, discontinuous short events. (h) SW-2 showing that individual ages overlap within error despite sharp contacts between veins, indicating intermittent  $\text{CO}_2$  degassing events over very short period of time. (i) Sample SW-3 also shows overlapping ages of four individual veins. (j) SW-4 provides mainly older ages of  $142 \pm 2.9$  and  $141 \pm 14$  ka, and age of  $35.6 \pm 1.9$  ka for younger veinlet again proving that vein formation is not continuous process, but result of amalgamation of various veinlets reflecting independent  $\text{CO}_2$  degassing events (note that this veinlet broke off sample). (k) Dated vein in sample BCS-H01 with age of  $22 \pm 0.6$  ka. (l) BCS-H02 with three veins with distinctly different ages indicating three punctuated events. (m) Single vein with age of  $35.9 \pm 0.1$  ka from sample BCS-H03. (For interpretation of the references to color in this figure legend, the reader is referred to the web version of this article.)

injected to remove atmospheric CO<sub>2</sub>. The water samples were acidified with phosphorus pentoxide in an autosampler to ensure complete release of CO<sub>2</sub> from acidified waters. CO<sub>2</sub> was then directly admitted to a continuous flow mass spectrometer (AP2003). The extracted CO<sub>2</sub> amounts represent the total content of dissolved carbon. The results are reported in ‰ units relative to the VPDB (Vienna Pee Dee Belemnite) international standard. The standard deviation of the <sup>13</sup>C/<sup>12</sup>C ratios was ±0.2‰.

### 3.3. Travertine vein samples

Vein samples consist of individual veinlets at the millimeter scale, which are separated from each other by terrigenous material (Fig. 4e–m). Calcite veins were cut and polished to remove any weathered surfaces, and then cleaned ultrasonically. The polished slabs were microdrilled for preliminary investigation using 1–2 mm drill bits. Based on initial U-series ages, a second set of calcite samples was obtained by grinding and drilling (for powders) or by cutting (for chips) the veins at measured distances perpendicular to growth from the wall rock. For avoiding contamination with host rock material, samples were taken at least 1 mm away from the vein walls. The samples were then used for U-series dating and also trace element and C–O–Sr isotope analyses.

U-series dating was carried out using a Nu Plasma multicollector inductively-coupled-plasma mass spectrometer (MC-ICP-MS) in the Radiogenic Isotope Facility (RIF) at University of Queensland (UQ) following chemical treatment procedures and MC-ICP-MS analytical protocols described elsewhere (Zhao et al., 2001; Clark et al., 2014). Powdered or chipped samples weighing 20–200 mg were spiked with a mixed <sup>229</sup>Th–<sup>233</sup>U tracer and then completely dissolved in double-distilled concentrated HNO<sub>3</sub>. After digestion, each sample was treated with H<sub>2</sub>O<sub>2</sub> to decompose trace amounts of organic matters (if any) and to facilitate complete sample-tracer homogenization. U and Th were separated using conventional anion-exchange column chemistry using Bio-Rad AG 1-X8 resin. After stripping off the matrix from the column using double-distilled 7 N HNO<sub>3</sub> as eluent, 3 ml of a 2% HNO<sub>3</sub> solution mixed with trace amount of HF was used to elute both U and Th into a 3.5 ml pre-cleaned test tube, ready for MC-ICP-MS analyses, without the need for further drying down and re-mixing. After column chemistry, the U-Th mixed solution was injected into the MC-ICP-MS through a DSN-100 desolvation nebuliser system with an uptake rate of ~0.12 ml/min. U–Th isotopic measurements were performed on the MC-ICP-MS using a detector configuration to allow simultaneous measurements of both U and Th isotopes (Clark et al., 2014). The <sup>230</sup>Th/<sup>238</sup>U and <sup>234</sup>U/<sup>238</sup>U activity ratios of the samples were calculated using the decay constants given in Cheng et al. (2000). The non-radiogenic <sup>230</sup>Th was corrected using an assumed bulk Earth atomic <sup>230</sup>Th/<sup>232</sup>Th ratio of  $4.4 \pm 2.2 \times 10^{-6}$  which requires minimal <sup>230</sup>Th/<sup>238</sup>U-age corrections to account for initial <sup>230</sup>Th in samples with <sup>230</sup>Th/<sup>232</sup>Th activity ratios higher than 20 as typical for most of our samples. U-series ages were calculated using Isoplot/Ex 3.75 (Ludwig, 2012).

Sr isotopic ratios were measured on a VG Sector-54 thermal ionization mass spectrometer (TIMS) in the RIF laboratory. They were corrected for mass discrimination using a <sup>86</sup>Sr/<sup>88</sup>Sr ratio of 0.1194. National Institute of Standards and Testing (NIST) SRM-987 Sr-isotope standard was used to monitor instrument drift and bias. Repeated analyses (no data outlier exclusion) of SRM-987 from January to May 2012 yielded an average <sup>87</sup>Sr/<sup>86</sup>Sr value of  $0.710222 \pm 0.000020$  ( $2\sigma$ ), which was used to calibrate against the laboratory's previous long-term mean of  $0.710249 \pm 0.000028$  ( $2\sigma$ ) for all samples.

Carbonate C and O isotope ratio analyses were conducted in the Stable Isotope Geochemistry Laboratory at UQ. Pure calcite samples (3–4 mg, powdered) were analyzed using an Isoprime Dual

Inlet Isotope Ratio Mass Spectrometer (DI-IRMS) with a multiprep device attached. Samples were reacted with orthophosphoric acid at 90 °C for 1000 s. Stable isotope analytical results are reported in per mil (‰) relative to V-SMOW (Vienna Standard Mean Ocean Water) and V-PDB for oxygen and carbon with analytical uncertainties better than ±0.2‰ ( $2\sigma$ ) for both  $\delta^{13}\text{C}$  and  $\delta^{18}\text{O}$ . The results were calibrated against NBS-19 and NBS-18, analyzed as unknowns in addition to an internal standard.

## 4. Structural geology

The mapped faults shown in Fig. 2 formed as steep normal faults in the Neoproterozoic (Krieg et al., 1991; Paul et al., 1999). Seismic profiles and field mapping by Adlam and Kuang (1988) showed that the faults cut through Eromanga Basin sediments and display positive flower structures. These authors also showed that the faults control the travertine deposits. Love et al. (2013) reported preliminary travertine U-series ages and also concluded that the travertines indicate neotectonic activity in south-central Australia.

Fault-related fracture systems in travertine deposits and their wallrocks can be grouped into shear fractures (Fig. 5a) and extension fractures (Fig. 5b). The two shear fracture sets strike ~60° and 130° and the extension fractures strike E–W. Both fractures sets are subvertical.

We collected fault-slip data from six localities along various strands of the NFZ (Fig. 2) and data plots are shown in Fig. 5. Some of the data (SA3 through SA5) are from the young travertine deposits (Fig. 4b) and must therefore have a young age. The remaining three data sets are from faults that extend from the travertine deposits into Eromanga sediments and basement (see above). In general, the data comprise near-vertical, NW-striking, sinistral strike-slip faults, a minor set of conjugated steep, NE-striking, dextral oblique reverse faults, a few N–S-striking reverse, and local locally E–W-striking normal faults. The derived extension axes all have a subhorizontal N–S orientation, whereas five out of six shortening axes are subhorizontal in the E–W direction with the shortening axis of the SA3 data set being subvertical. Eigenvalues of the data suggest constrictional to plane strain geometries (Table S1).

Despite the fact that the six data sets differ from each other and have been collected in different rock types, computed shortening and extension directions are consistent and provide an approximately E–W-trending shortening and a N–S-trending extension direction (Supplementary Table S1, Fig. 5). The derived shortening and extension axes indicate that faulting along the NW-striking steep faults has sinistral kinematics. The orientations of the travertine-filled shear fracture sets confirm an E–W-trending shortening and N–S-trending extension axes and, together with the extension fractures geometrically support sinistral strike-slip faulting on NW-striking faults (Fig. 5a, b). The fracture orientations also demonstrate that travertine deposition is tectonically controlled. Given that the displacements on the minor faults from which we collected the fault slip data are small, we infer that no significant deformation-related rotations occurred and that the shortening directions we derived from fault-slip analysis are parallel to the maximum horizontal compressive stress ( $S_{H\max}$ ). It follows that the collected structural data fit into the current intra-plate stress field (Reynolds et al., 2002; Hillis and Reynolds, 2000; Dyksterhuis and Müller, 2008). The structural data also agree with the strain directions obtained from focal-plane solutions (Hillis et al., 2008). Therefore, our structural data are characteristic for the neotectonic evolution of the region and can be linked to the emplacement of the travertine deposits.

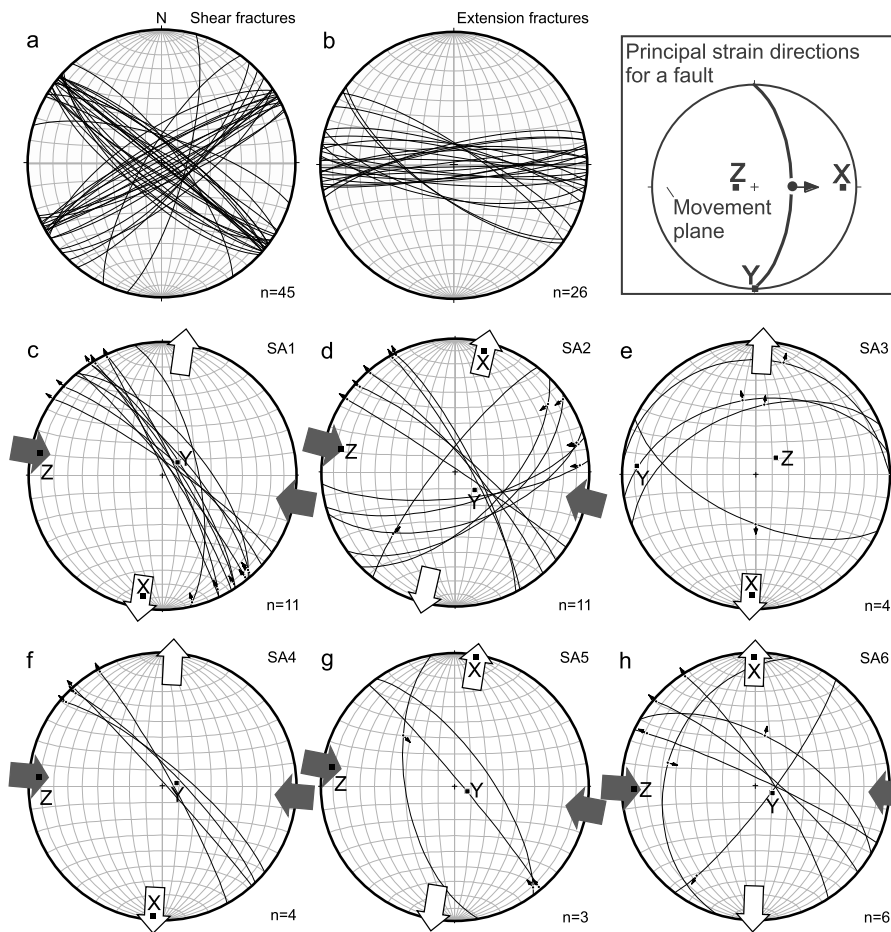


**Fig. 5.** Fracture geometry and kinematic data from NFZ. Diagrams in (a) and (b) show great circles of fracture planes, diagrams in (c–h) show great circle of fault plane and projected trace of slickenside lineation in lower-hemisphere equal-area projection; principal strain axes ( $X > Y > Z$ ) are shown, deduced extension directions ( $X$ ) indicated by arrows; outcrop number indicated on upper right and located in Fig. 2. Inset: graphical construction of principal incremental shortening and extension axes for given fault; movement plane of fault perpendicular to fault plane containing unit vector parallel to direction of accumulated slip and normal vector to fault plane; shortening and extension axes at  $45^\circ$  to fault plane. (a) Shear fractures in carbonic spring deposits depicting two subvertical fractures sets striking  $\sim 60^\circ$  and  $\sim 130^\circ$ , bisector of acute angle of two sets at  $\sim 95^\circ$  supplies shortening axes. (b) Orientation of subvertical extension fractures supplying average extension direction of  $\sim 5^\circ$ . (c) Outcrop SA1 characterized by simple set of NW-striking, steep sinistral strike-slip faults recording ENE-directed shortening. (d) Station SA2 showing set of conjugated NW-striking sinistral and NE-striking dextral faults recording ENE-directed shortening. (e) Set SA3 showing E-W-striking normal faults. (f) Outcrop SA4 shows similar data set as SA1 with simple set of NW-striking, steep, sinistral strike-slip faults recording ENE-directed shortening. (g) SA5 with small data set that is similar to SA1 and SA4. (h) Station SA6 showing conjugated set of sinistral and dextral strike-slip faults, fault set similar to SA2.

## 5. U-series dating

We dated 26 travertine veins using the U-series method (Figs. 3, 6, Table 1 and Supplementary Table S2). The ages indicate that the travertine deposits formed in the late Quaternary between  $354 \pm 7$  and  $1.19 \pm 0.02$  ka ( $2\sigma$  errors). The oldest age of  $354 \pm 7$  ka is from Eromanga sediment exposed in the Willouran Range (Fig. 2, 4e), while the ages for Warburton Spring ( $21.4 \pm 0.6$  to  $12.4 \pm 1.1$  ka) (Fig. 4f), Strangways Spring ( $142 \pm 2.9$  ka to  $1.19 \pm 0.02$  ka) (Fig. 4g–j) and Blanche Cup Spring ( $39.1 \pm 2.2$  ka and  $9.05 \pm 0.27$  ka) (Fig. 4k–m) yielded distinctly younger ages, most of which cluster between 26 and 1 ka. Calcite slickensides from a small-scale fault surface at Blanche Cup Spring were dated at  $24.6 \pm 3.1$  ka (Fig. 4b).

Structural evidence of veining in outcrop and hand specimens combined with U-Th age data show that each carbonate vein formation event was rapid, similar to vein formation in seismically active areas in Turkey and Israel (Uysal et al., 2007, 2011; Nuriel et al., 2011; Ünal-İmer et al., 2016). As is the case for vein growth in the latter two regions, samples from the NFZ show parallel oriented crystal fibers that grew perpendicular to the vein walls (Fig. 4e, g, h, i, k). Individual veinlets are distinctive with sharp

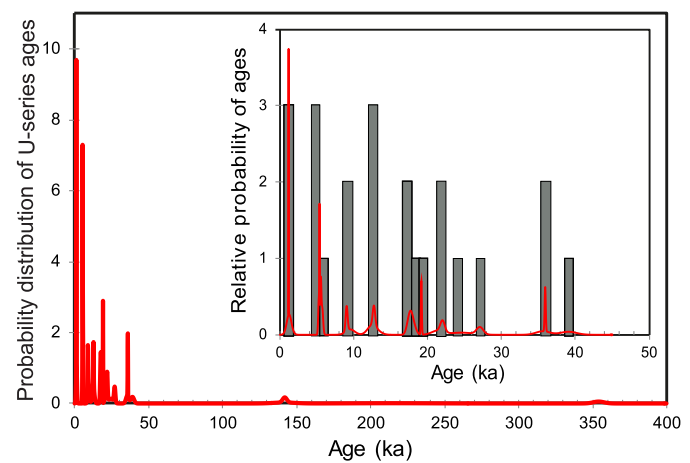


**Fig. 6.** U/Th age vs probability distribution of ages for travertine veins showing clustering of ages younger than  $\sim 26$  Ma. Inset shows probability distribution of U-series ages with histograms (in grey) for ages. Curves show relative probabilities calculated using Isoplot 7 for Excel (Ludwig, 2012).

**Table 1**

Chemical composition of dissolved and free gas and isotopic composition of helium and carbon.

	$\text{CO}_2$	$\delta^{13}\text{C}_{\text{TDC}}$	$R/R_a$	${}^4\text{He}/{}^{20}\text{Ne}$	$R/R_{ac}$	${}^{230}\text{Th}/{}^{238}\text{U}$ age (ka) $\pm 2\sigma$	$({}^{234}\text{U})/{}^{238}\text{U}$	$\delta^{18}\text{O}$ mineral	$\delta^{13}\text{C}$ mineral	Sr content (ppm)	${}^{87}\text{Sr}/{}^{86}\text{Sr} \pm 2\sigma$
<i>Springs along Northwest Fault</i>											
Free gas (vol%)											
Bubbler spring	1.78	-10.13	0.07 ± 0.0012	109.9	0.07						
Coward spring	7.17	-11.54	0.07 ± 0.0020	269.0	0.07						
Dissolved gas (cc <sub>gas</sub> /L <sub>H<sub>2</sub>O</sub> )											
Bubbler spring	67.02	-13.87	0.08 ± 0.0014	304.9	0.08						
Bubbler spring	56.09		0.07 ± 0.0012	109.9	0.07						
Blanche cup spring	15.90		0.07 ± 0.0008	16.7	0.06						
Strangways spring	71.18	-14.3	0.03 ± 0.0008	100.1	0.03						
Coward spring	70.73	-9.23	0.07 ± 0.0020	269.0	0.07						
<i>Bores away from Northwest Fault</i>											
Dulkannina	42.45	-7.21	0.03 ± 0.0007	36.8	0.03						
Bore											
Clayton Bore	18.16	-8.01	0.02 ± 0.0007	151.8	0.02						
<i>Travertine samples</i>											
BCS-H01				22 ± 0.6	12.48	24.3	-2.2	18069	0.714568 ± 0.000010		
BCS-H02a				9.05 ± 0.27	16.18	25.2	-2.0	21405	0.714380 ± 0.000006		
BCS-H02a-2				12.7 ± 0.3	7.10						
BCS-H02b				17.4 ± 0.6	16.10	25.5	-2.2	22120	0.714352 ± 0.000011		
BCS-H03				35.9 ± 0.1	10.78	24.8	-3.5	22772	0.714336 ± 0.000009		
BCS-V01				27.1 ± 0.9	19.24						
BCS-V02				39.1 ± 2.2	12.46	24.9	-2.4				
BCS-V03				9.53 ± 1.23	18.40	23.5	-3.6	7958.6	0.714640 ± 0.000014		
BCS-slickenside				24.6 ± 3.1	11.62	26.2	-2.7				
SW-1 B1				19.2 ± 0.1	19.26	24.7	-6.7	2424.0	0.714488 ± 0.000007		
SW-1 B2				18.1 ± 0.7	18.13						
SW-1 T				17.7 ± 0.5	19.44						
SW-2 B				1.29 ± 0.74	13.08	24.9	-3.9	2377.7	0.713180 ± 0.000009		
SW-2 T				1.24 ± 0.57	14.47						
SW-2 T2				1.19 ± 0.02	17.24						
SW-3 040				5.75 ± 0.24	11.84	24.5	-4.8	1802.5	0.712844 ± 0.000010		
SW-3 145				5.56 ± 0.13	11.62						
SW-3 150				5.39 ± 0.06	12.07						
SW-3 160				5.3 ± 0.18	10.93						
SW-4a B				141 ± 14	5.915	26.0	-3.2	1181.9	0.713173 ± 0.000021		
SW-4a T				142 ± 2.9	6.108						
SW-4b				35.6 ± 1.9	14.80						
SW-5					5.454	25.1	-4.6				
SW-6					4.431	25.8	-3.1				
WS-2-002				12.9 ± 1.4	3.341	23.8	-5.7		0.713178 ± 0.000011		
WS-2-005				12.4 ± 1.1	1.076						
WS-2-007				21.4 ± 1.6		24.3	-4.9	11421	0.714491 ± 0.000011		
WR				354 ± 7		24.3	-3.1	9631.7			

$R/R_{ac}$  recalculated values after removal of atmospheric contribution following Hilton (1996).  ${}^4\text{He}/{}^{20}\text{Ne} = 0.267$  (Holocher et al., 2002). O and C reported in ‰ V-SMOW and ‰ V-PDB. WS = Warburton Spring; SW = Strangways Spring; BCS = Blanche Cup Spring; WR = Willouran Range. Note: T, B in sample ID's refer to top (T) and bottom (B) of calcite vein; sample ID's with number suffixes (SW-3, WS-2) refer to distances in mm from host rock.

contacts and abrupt termination of crystal growth as well as alignment of new carbonate fibers along interfaces with earlier veinlet generations. Crystal growth terminated before new crystals formed. Thin layers of brown–yellow iron staining or greyish–black coloring (possibly organic-rich material) occur between boundaries of separate calcite bands as traces of terminated calcite formation (Fig. 4g, i) representing a growth hiatus between the two growth phases. This is well shown in sample SW-1 (Fig. 4g) where each calcite vein formed during a single veining event, with no post-dilation continuous growth for a significant period of time. The growth hiatus indicates episodic growth with two discrete calcite growth events at  $19.2 \pm 0.1$  ka and  $18.1 \pm 0.7/17.7 \pm 0.5$  ka demonstrating that the ages represent two separate veining events. The same is true for samples BCS-H02 and SW-4 (Fig. 4l, j), which also provide strong evidence of vein growth during periodic, discontinuous and short events. Nonetheless, some samples (e.g. SW-2, SW-3) have veins with sharp contacts, which yielded overlapping U-series ages,

indicating intermittent CO<sub>2</sub> degassing events over very short periods (Fig. 4h, i).

Because of these textural relationships and because the individual U/Th ages are generally distinctly different from each other (Fig. 4f, g, k), the ages represent separate veining events rather than continuous vein formation over the last ~35 ka. The majority of the U-series ages of the carbonate veins cluster between 40 and 1 ka (Fig. 6) with most ages (a total of 7) between 6 and 1 ka. A probability distribution of the ages shows major veining events at 35.9 ka, 26.4 ka, 21.6 ka, 19.1 ka, 17.6 ka, 12.6 ka, 9 ka, 5.4 ka, and 1.2 ka (Fig. 6). The age clusters occur every ~3–5 ka between 26.4 ka and 1.2 ka. Another conspicuous feature of the U-series data is the significantly high  ${}^{234}\text{U}/{}^{238}\text{U}$  activity ratios of the travertines (Table 1). Theoretically, this activity ratio should be equal to unity in rocks and waters (Prescott and Habermehl, 2008).

## 6. Isotope geochemistry

### 6.1. Data

We describe data of dissolved and free gas samples from springs along the NFZ, and from two artesian bores (Dulkannina and Clayton bores in Fig. 2) more than ~50 km away from the NFZ. We define the He isotopic signature of the gas samples in particular because  $^3\text{He}$  is a tracer for mantle-derived fluids. We then present geochemical data from the travertine vein material and finally interpret our data.

#### 6.1.1. Gas samples

All but two gas samples have been extracted from waters having outlet temperatures between 24 and 62 °C, pH between 6.1 and 7.6 and electrical conductivity >1000 mS/cm. The gas-chromatographic analyses (Supplementary Table S3) show that  $\text{CO}_2$  ranges from 15.9 to 71.18 cm<sup>3</sup>/L<sub>H<sub>2</sub>O</sub> at standard pressure and temperature (STP) and is by far the most abundant component of the dissolved gas phase. The concentrations of the other gas components are an order of magnitude lower.  $\text{N}_2$  ranges from 9.01 to 19.76 cm<sup>3</sup>/L<sub>H<sub>2</sub>O</sub>STP,  $\text{O}_2$  between 0.06 and 2.1 cm<sup>3</sup>/L<sub>H<sub>2</sub>O</sub>STP,  $\text{CH}_4$  from 0.29 to 547.37 cm<sup>3</sup>/L<sub>H<sub>2</sub>O</sub>STP and He is ranging between  $4.51 \times 10^{-3}$  and  $1.39 \times 10^{-1}$  cm<sup>3</sup>/L<sub>H<sub>2</sub>O</sub>STP.

Our samples are enriched in atmospheric components as expected for any dissolved gas, along with non-atmospheric gaseous species. The concentration of oxygen is very low and always below its content in air-saturated water (ASW) of 4.8 cm<sup>3</sup>/L<sub>H<sub>2</sub>O</sub>STP. In contrast,  $\text{N}_2$  is usually well above the ASW equilibrium (Table S3). The most abundant non-atmospheric component is  $\text{CO}_2$ , which in water samples has values well above the ASW equilibrium of 0.24 cm<sup>3</sup>/L<sub>H<sub>2</sub>O</sub>STP (Weiss, 1974).  $\text{CO}_2$  concentrations in samples from the NFZ are higher than those from the bore samples away from the fault (Table 1).  $\text{CH}_4$  ranges from 0.01 to 0.59 cm<sup>3</sup>/L<sub>H<sub>2</sub>O</sub>STP and is thus highly depleted in springs from the NFZ, but substantially enriched (290.77–547.37 cm<sup>3</sup>/L<sub>H<sub>2</sub>O</sub>STP) in bores away from the NFZ. The isotopic composition of total dissolved carbon ( $\delta^{13}\text{C}_{\text{TDC}}$ ) ranges between  $-13.87$  to  $-9.23\text{\textperthousand}$  for samples from the NFZ, and  $-8.01$  to  $-7.21\text{\textperthousand}$  for the bore samples.

**6.1.1.1. Isotopic composition of helium** Table 1 lists the results of helium isotope analyses normalized to atmosphere and expressed as  $R/R_a$  values (where  $R = ^3\text{He}/^4\text{He}$  sample;  $R_a =$  atmospheric  $^3\text{He}/^4\text{He}$  ratio =  $1.4 \times 10^{-6}$ ). For testing whether our samples are contaminated by ASW during recharge of the surface water into the hydrothermal Great Artesian Basin groundwater system or by air during sampling, we measured  $^4\text{He}/^{20}\text{Ne}$  ratios. In dissolved gas from the artesian bore samples,  $^4\text{He}/^{20}\text{Ne}$  ratios range between 16.7 and 304.9 (Table 1), which compared to the ratio of 0.267 for air-saturated water (Holocher et al., 2002) indicates a negligible contribution of atmospheric  $^3\text{He}$  to our bore samples. Considering that  $^3\text{He}$  either comes from the mantle or the atmosphere, we removed the atmospheric source based on the measured  $^4\text{He}/^{20}\text{Ne}$  ratios assuming all  $^{20}\text{Ne}$  is of atmospheric provenance. The  $^3\text{He}/^4\text{He}$  values corrected for air contamination ( $R/R_{ac}$ ) range between 0.06 and 0.08 (note that only Strangways Spring has a lower value of 0.03) and indicate a contribution of mantle  $^3\text{He}$  ( $R/R_{ac} > 0.02$  indicates an input of mantle derived He; Ballentine et al., 2002). Because the amount of atmospheric  $^3\text{He}$  in all our samples is negligible,  $R/R_a$  and  $R/R_{ac}$  values are identical (Table 1).

$^3\text{He}/^4\text{He}$  ratios of water samples from the NFZ differ significantly from those of artesian bores away from the NFZ. Artesian bore samples display values of 0.02–0.03 for  $R/R_{ac}$ , whereas samples from the NFZ range between 0.06 and 0.08 for  $R/R_{ac}$ .

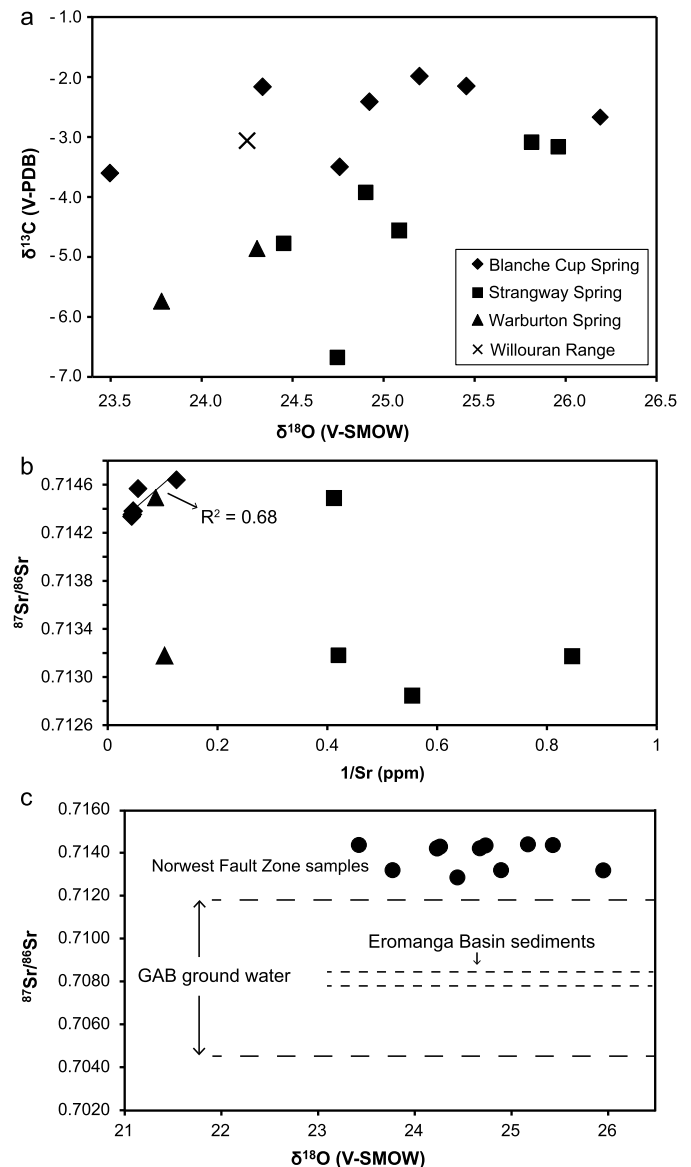


**Fig. 7.** O-C-Sr isotope variation diagrams. (a)  $\delta^{13}\text{C}$  vs  $\delta^{18}\text{O}$  of calcite vein samples showing weak positive correlation suggesting significant and transient  $\text{CO}_2$ -water phase separation by  $\text{CO}_2$  degassing resulting from rapid fluid-pressure decrease (Bergfeld et al., 2012). (b) Relation between Sr content and  $^{87}\text{Sr}/^{86}\text{Sr}$  for travertine veins; two-component mixing indicated by linear relation for samples from Blanche Cup Spring, whereas scatter of other samples indicating mixing of multiple sources. (c)  $^{87}\text{Sr}/^{86}\text{Sr}$  vs  $\delta^{18}\text{O}$  for all travertine veins compared to  $^{87}\text{Sr}/^{86}\text{Sr}$  values of Eromanga Basin sediments and Great Artesian Basin (GAB) groundwater.

(Table 1). Love et al. (2013) also showed increased  $R/R_{ac}$  values of 0.09 for Bubbler Spring.

#### 6.1.2. Travertine samples

Travertine samples have  $\delta^{13}\text{C}_{\text{mineral}}$  and  $\delta^{18}\text{O}_{\text{mineral}}$  values of  $-6.7$  to  $-2\text{\textperthousand}$  and 23.5 to 26.2‰, respectively (Fig. 7a, Table 1 and Supplementary Table S4). Estimated aqueous isotopic values for  $\delta^{13}\text{C}$  and  $\delta^{18}\text{O}$  were calculated using the calcite- $\text{CO}_2$  fractionation (Chacko et al., 1991) and a temperature of 30 °C measured for the spring waters. For samples collected at Bubbler Spring and Blanche Cup Spring, water values range from  $-13.5$  to  $-119.9\text{\textperthousand}$  ( $\delta^{13}\text{C}$ ) and  $-3.9$  to  $-1.2\text{\textperthousand}$  ( $\delta^{18}\text{O}$ ). For travertine veins at Strangways Spring,  $\delta^{13}\text{C}_{\text{CO}_2}$  is more depleted and ranges from  $-16.6$  to  $-13\text{\textperthousand}$ , while estimated water  $\delta^{18}\text{O}$  values for these travertines range from  $-3.6$  to  $-1.4\text{\textperthousand}$  and are similar to values from Bubbler and Blanche

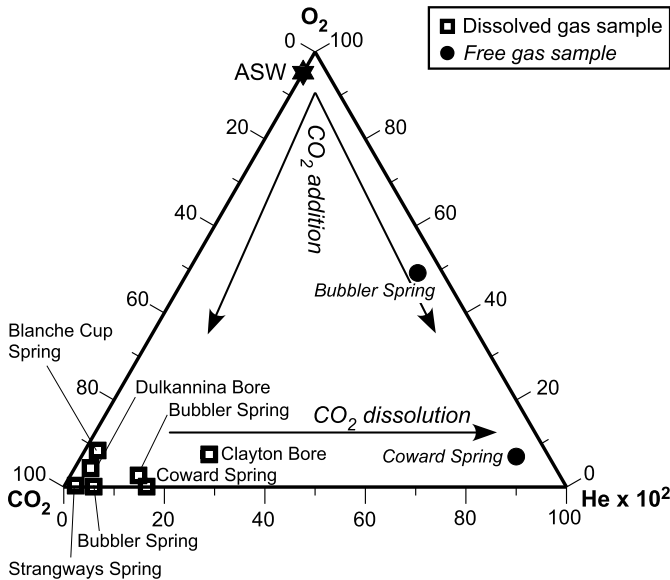


**Fig. 8.**  $\text{CO}_2$ -He-O<sub>2</sub> relationships for free and dissolved gas; arrows show  $\text{CO}_2$  removal (dissolution) and  $\text{CO}_2$  addition due to interaction with Great Artesian groundwater. Samples from NFZ (Blanche Cup, Bubbler, Strangways Spring and Coward Spring) and bores away from NFZ (Dulkannina and Clayton bores) high in  $\text{CO}_2$ , whereas free gas samples from Bubbler and Coward Spring distinctly depleted in  $\text{CO}_2$  due to dissolution of  $\text{CO}_2$  and relative enrichment in He. ASW = air-saturated water.

Cup Spring (Keppel et al., 2013). (Note that  $\delta^{13}\text{C}_{\text{CO}_2}$  refers to the original  $\text{CO}_2$  before travertine precipitation.)

The  $^{87}\text{Sr}/^{86}\text{Sr}$  ratios of travertine vein samples (Table 1) are shown in Fig. 7b, c in comparison to the Sr isotope values of waters from the Great Artesian and Eromanga basins. The travertine samples show a range in  $^{87}\text{Sr}/^{86}\text{Sr}$  ratios (0.712844–0.714568), which are significantly higher than  $^{87}\text{Sr}/^{86}\text{Sr}$  ratios of representative Eromanga Basin sediments and the most radiogenic values for Great Artesian Basin waters (cf. Collerson et al., 1988). The travertine Sr isotope ratios are also much higher than those reported for modern brines and salts from the Lake Frome basin southeast of Lake Eyre (Ullman and Collerson, 1994) (Fig. 7c). The most radiogenic values are from samples at Blanche Cup Spring (Fig. 7).

## 7. Interpretation of geochemical data

### 7.1. $\text{CO}_2$ and mantle $^3\text{He}$ in the Norwest fault zone

The geochemical data of the gas samples show a significant amount of deep-seated gas components. To verify the presence of mantle-derived volatiles in a crustal environment is difficult, especially when the mantle is overlain by 30–35 km of highly radiogenic rock (Neumann et al., 2000), which masks mantle volatiles through mixing with large amounts of radiogenic crustal volatiles (Italiano et al., 2014). In a  $\text{CO}_2$ -He-O<sub>2</sub> diagram (Fig. 8), the sample points of dissolved gas are close to the  $\text{CO}_2$  vertex, while the two samples from the artesian Dulkannina and Clayton bores away from the NFZ show significant He enrichment besides a relatively low  $\text{CO}_2$  content. The results are explained by the trends shown by the arrows in Fig. 8: Highly dissolved  $\text{CO}_2$  is consistent with up-flow of deep  $\text{CO}_2$ -rich volatiles (either of crustal or mantle origin); low  $\text{CO}_2$  content is best explained by gas/water interactions responsible for variable  $\text{CO}_2$  dissolution and He enrichment. Any large  $\text{CO}_2$  content means a significant contribution of volatiles that cannot have originated in the basement. Crust-derived  $\text{CO}_2$  can result from calcite devolatilization of carbonate rocks and is characterized by positive isotopic values. The carbon isotopic composition ( $\delta^{13}\text{C}_{\text{CO}_2}$ ) between  $-11.54$  and  $-10.13\text{\textperthousand}$ ;  $\delta^{13}\text{C}_{\text{TDC}}$  ranging

between  $-14.03\text{\textperthousand}$  and  $-8.1\text{\textperthousand}$ ) rules out a major contribution of organic carbon, and thus favors mantle degassing (see Italiano et al., 2014 for further details).

For dissolution of  $\text{CO}_2$ , two different and separate effects have to be considered: (1) enrichment of  $\text{CO}_2$  in the dissolved gas phase due to groundwater interaction with a  $\text{CO}_2$ -rich gas phase, and (2)  $\text{CO}_2$  loss due to re-equilibration within the groundwater. As a consequence of the first effect, the  $\text{CO}_2$  content of the dissolved gas phase increases and, contrastingly, its concentration in the dissolved gas phase decreases because of the second effect. After simple  $\text{CO}_2$  dissolution ( $\text{CO}_{2g} \rightarrow \text{CO}_{2aq}$ ) an equilibrium is established between the dissolved  $\text{CO}_2$  and  $\text{H}_2\text{CO}_3$ , carbonic acid, ( $\text{CO}_{2aq} + \text{H}_2\text{O} \rightarrow \text{H}_2\text{CO}_{3aq}$ ). Although only about 1% of the dissolved  $\text{CO}_2$  exists as  $\text{H}_2\text{CO}_3$ , the weak carbonic acid dissociates:  $\text{H}_2\text{CO}_3 \rightarrow \text{H}^+ + \text{HCO}_3^-$  (solubility product =  $4.2 \times 10^{-7}$ ;  $T = 298$  K) and  $\text{HCO}_3^- \rightarrow \text{H}^+ + \text{CO}_3^{2-}$  (solubility product =  $4.8 \times 10^{-11}$ ;  $T = 298$  K). As  $\text{CO}_2$  dissolves, the carbonate anion ( $\text{CO}_3^{2-}$ ) forms and interacts with cations (i.e.  $\text{Ca}^{2+}$  and  $\text{Mg}^{2+}$ ). These interactions induce  $\text{CO}_2$  loss because of the low solubility of  $\text{CaCO}_3$  (solubility product constant:  $5 \times 10^{-9}$ ;  $T = 298$  K) and  $\text{MgCO}_3$  (solubility product constant:  $6.82 \times 10^{-6}$ ;  $T = 298$  K). These processes change both the chemical and isotopic composition of  $\text{CO}_2$  as the heavier carbon ( $^{13}\text{C}$ ) is preferentially enriched in the carbonate anion. Repeated groundwater interaction, or interaction with large water/gas ratios, seriously modifies either the original  $\text{CO}_2$  content or its carbon isotope ratio. The amount of dissolved gas extracted may underestimate the dissolved  $\text{CO}_2$ , whose carbon isotopic composition is characterized by lower  $\delta^{13}\text{C}$  values than the pristine  $\text{CO}_2$ . The  $\delta^{13}\text{C}_{\text{TDC}}$  values recorded for the NFZ dissolved carbon indicate higher  $\delta^{13}\text{C}$  values of the original gaseous  $\text{CO}_2$ .

The  $^3\text{He}/^4\text{He}$  ratios in the NFZ samples are significantly higher than those from artesian bores away from the NFZ. The  $^3\text{He}/^4\text{He}$  ratios in radiogenic basement rocks should have  $R/R_a$  of  $\leq 0.01$  (Ballentine et al., 2002). Artesian bore samples display almost pure radiogenic values, whereas NFZ-related springs show up to triple values ( $R/R_{ac}$  0.06–0.08, except Strangways Spring) (Table 1) with a  $^3\text{He}$  content of  $10^{-8} \text{ cm}^3/\text{L}_{\text{H}_2\text{O}}\text{STP}$  and thus two orders of magnitude higher than the samples away from the NFZ. Moreover, the loss of  $\text{CO}_2$  relatively increases the concentration of the less soluble species, thus the dissolved  $^3\text{He}$  content ranges from  $4.4 \times 10^{-10}$  to  $1.5 \times 10^{-8}$ , and is thus two to four orders of magnitude higher than ASW.

The radiogenic  $^3\text{He}/^4\text{He}$  ratios can be modified by  $^3\text{He}$  addition to volatiles and groundwater from a few other natural sources: tritium decay, entrapment of air bubbles, and influx of mantle He. Detectable contributions from tritium decay can be ruled out because of low tritium contents in the Great Artesian Basin (Kulongoski et al., 2003, 2005). Air bubble entrapment does not contribute because the high  $^4\text{He}/^{20}\text{Ne}$  ratios show that the presence of  $^3\text{He}$  in the air is negligible. Li could produce  $^3\text{He}$  through thermal neutron capture. However, in the same granite source,  $^4\text{He}$  is contemporaneously produced by radioactive decay of U and Th. The U and Th content of granites in the region are 10.3 ppm and 45.7 ppm (Heier and Rhodes, 1966; Collins et al., 1982) yielding an estimated total  $^4\text{He}$  content of  $1.88 \times 10^8$  atoms/a/g. Given an average Li content of 15 ppm (Teng et al., 2009), the  $^3\text{He}$  and  $^4\text{He}$  production rates yield an isotopic ratio of 0.007 Ra (Ballentine et al., 2002) that matches a typical radiogenic He isotopic composition of  $<0.01 R_a$  (Ballentine et al., 2002). It is noteworthy that a  $^4\text{He}$  production rate of  $6.97 \times 10^{-12}$  atoms/s, which equals  $\sim 2 \times 10^{18}$  atoms/Ma/km<sup>3</sup> of basement rock represents a huge amount of  $^4\text{He}$  that can be stripped from micro-fractured basement if a carrier gas like  $\text{CO}_2$  is available.

Fig. 9 shows the  $^3\text{He}$  vs  $^4\text{He}$  contents of the NFZ samples. All samples, i.e. dissolved and free gas, plot along the 1% mantle/radiogenic He mixing line indicating a mantle volatile flux. Even if

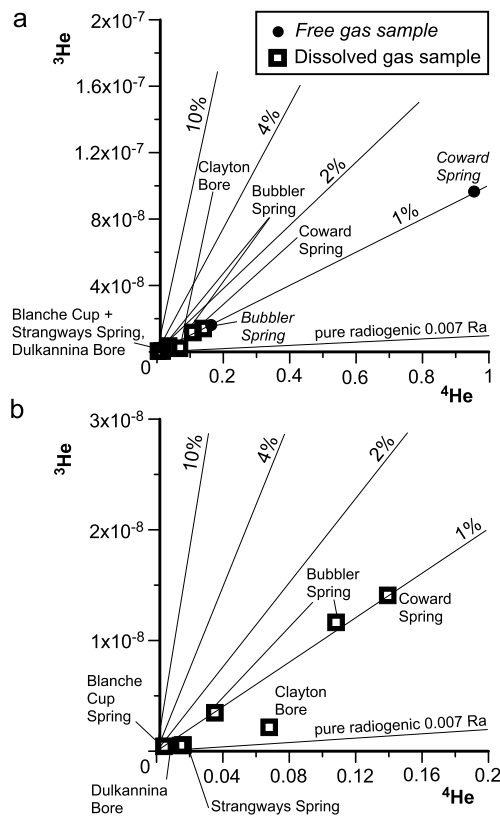


**Fig. 9.**  ${}^3\text{He}$  vs  ${}^4\text{He}$  contents of NFZ samples. Mixing lines represent variable addition of mantle  ${}^3\text{He}$  (assuming subcontinental mantle characterized by  $6.5 R_a$ ) to radiogenically produced  ${}^4\text{He}$  in crystalline basement ( $0.007 R_a$ ). (a) All samples. (b) Same plot with dissolved gas samples shown at different scale.

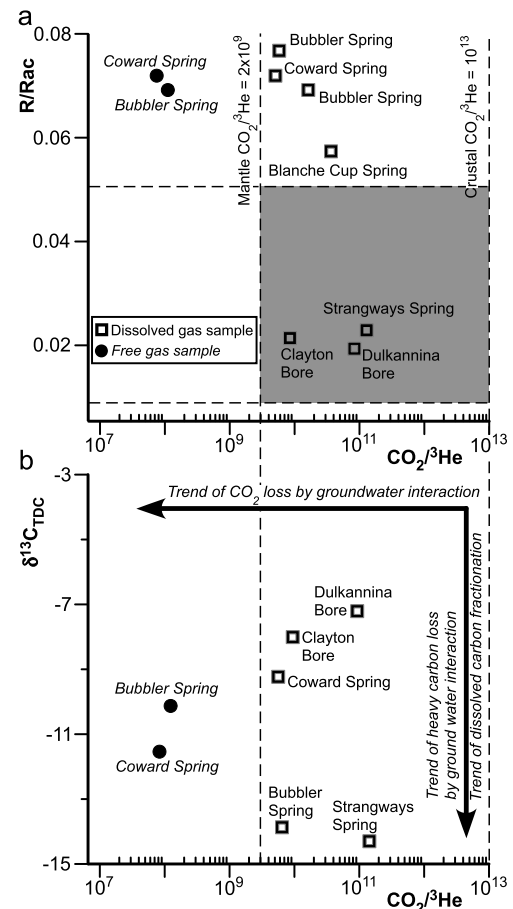
this flux is small, it is in agreement with the proposed mantle He flux feeding the aquifers by a diffusive process (Kulogoski et al., 2003, 2005). The assumption of the same mantle end member of  $6.5 R_a$  (Italiano et al., 2014) requires a mixing of 2% to fit the NFZ samples.

Fig. 10 plots the  $\text{CO}_2/{}^3\text{He}$  ratios of both dissolved and free gas against the isotopic composition of He and C.  $\text{CO}_2/{}^3\text{He}$  ratios are commonly used to constrain the origin of  $\text{CO}_2$ , to evaluate the extent that mantle volatiles contribute to the gas phase, as well as element fractionation between He and  $\text{CO}_2$ . The  $\text{CO}_2/{}^3\text{He}$  ratios in the dissolved gas samples from the NFZ display a range of three orders of magnitude (from  $5 \times 10^9$  to  $1.2 \times 10^{11}$ ), are by two orders of magnitude lower than in the free gas samples ( $0.7$  to  $1.1 \times 10^8$ ; Supplementary Table S3), and are similar to ratios proposed for the mantle ( $2 \times 10^9$  for MORB; Marty and Jambon, 1987).

Because  ${}^3\text{He}/{}^4\text{He}$  ratios can only be modified by admixture of He with a different isotopic signature, i.e. from a different reservoir, the coexistence of low  ${}^3\text{He}/{}^4\text{He}$  ratios (masked by a high crustal  ${}^4\text{He}$  component) and low, mantle-like  $\text{CO}_2/{}^3\text{He}$  ratios, suggest that either chemical  $\text{CO}_2$  fractionation or mixing of crustal and mantle-derived He modified the  $\text{CO}_2/{}^3\text{He}$  ratio.

Fig. 10 shows those relatively high  $\text{CO}_2/{}^3\text{He}$  ratios for samples from the Dulkannina and Clayton bores, and also from Strangways Spring in the NFZ. The rest of the NFZ samples is distinctly enriched in  ${}^3\text{He}$  and has lower  $\text{CO}_2/{}^3\text{He}$  ratios supporting a mantle-derived  ${}^3\text{He}$  contribution in the NFZ samples. The decrease in  $\text{CO}_2/{}^3\text{He}$  ratios is consistent with the observed  $\text{CO}_2$  loss due to interaction with Great Artesian groundwater.

We maintain that it is not important how large the  ${}^3\text{He}$  mantle contribution is, but that it is critical to show that the mantle degasses and mantle volatiles contribute to the final composition of the vented fluids. Detecting a 1% contribution of mantle helium in



**Fig. 10.** (a) Plot of  $\text{CO}_2/{}^3\text{He}$  vs  $R/R_{ac}$ . Relatively high  $\text{CO}_2/{}^3\text{He}$  samples from Dulkannina and Clayton bores plot together with sample from Strangways Spring at NFZ, rest of NFZ samples distinctly enriched in  $R/R_{ac}$ ; free gas samples have distinctly lower  $\text{CO}_2/{}^3\text{He}$  ratios; grey rectangle covers range of radiogenic (crustal) He and mantle He to crustal  $\text{CO}_2/{}^3\text{He}$  ratios, note that only one single sample from NFZ plot in this field. (b)  $\text{CO}_2/{}^3\text{He}$  vs  $\delta^{13}\text{C}_{TDC}$ . Vertical downward facing arrow depicts fractionation trend of  $\delta^{13}\text{C}_{TDC}$  due to  $\text{CO}_2$  dissolution induced by interaction with Great Artesian Basin groundwater, heavy  $\delta^{13}\text{C}$  goes preferentially into fluid phase causing observed carbon fractionation and decreasing  $\delta^{13}\text{C}_{TDC}$  trend; horizontal arrow indicates  $\text{CO}_2$  induced loss by interaction with Great Artesian groundwater.

crust  $\sim 30$ – $35$  km thick and chiefly made up by highly radiogenic granites (Neumann et al., 2000) is not negligible and indicates that the NFZ is tapping the mantle.

## 7.2. Stable isotopes and ${}^{87}\text{Sr}/{}^{86}\text{Sr}$ ratios

TDC compositions of samples from the NFZ of  $-13.87$  to  $-9.23\text{\textperthousand}$  are similar to calculated  $\delta^{13}\text{C}$  values of water from which the travertines precipitated. These values are compatible with significant involvement of mantle  $\text{CO}_2$  ( $\delta^{13}\text{C}_{MORB} = -6.5 \pm 2.5\text{\textperthousand}$ ) with some minor organic component (cf. Boreham et al., 2001). The samples from the NFZ have increased  ${}^3\text{He}/{}^4\text{He}$  ratios (except the one from Strangways Spring) and higher  $\text{CO}_2$  content (up to 71ccSTP) than artesian well samples away from the fault (up to 42 cm $^3/\text{LH}_2\text{O}$ STP), indicating mantle  $\text{CO}_2$  as the carrier gas for  ${}^3\text{He}$  transport.

The  $\text{CO}_2/{}^3\text{He}$  vs  $\delta^{13}\text{C}$  diagram in Fig. 10b shows that carbon isotope fractionation ( $\delta^{13}\text{C}_{TDC}$ ) is due to  $\text{CO}_2$  loss induced by interaction with Great Artesian Basin groundwater. The heavy  $\delta^{13}\text{C}$  goes preferentially into the liquid phase and is responsible for the observed C fractionation depicting an increasing  $\delta^{13}\text{C}_{TDC}$  trend. This fractionation process is commonly observed in  $\text{CO}_2$ -rich waters (Italiano et al., 2009).

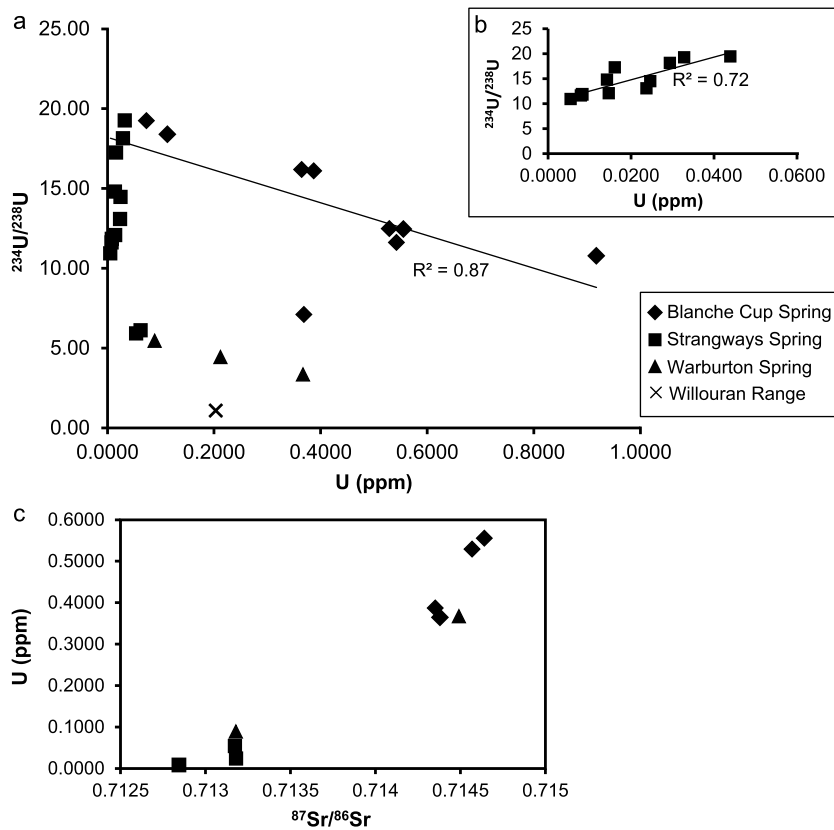


**Fig. 11.** Relation between U concentration and  $^{234}\text{U}/^{238}\text{U}$  for (a) all travertine veins, and (b) only for samples from Strangways Spring (two outliers, SW-4a B, SW-4a T, not plotted). (c) Relation between U content and  $^{87}\text{Sr}/^{86}\text{Sr}$  values of travertine veins.

In a  $^{87}\text{Sr}/^{86}\text{Sr}$  vs  $1/\text{Sr}$  (ppm) plot (Fig. 7b), samples from Blanche Cup Spring illustrate a linear two-component mixing line suggesting that the fluids from which calcite precipitated consist of two end members. Samples from other localities exhibit a more complex relation between Sr and  $^{87}\text{Sr}/^{86}\text{Sr}$  reflecting mixing of a variety of fluids with variable  $^{87}\text{Sr}/^{86}\text{Sr}$  ratios.  $^{87}\text{Sr}/^{86}\text{Sr}$  values of fault-related travertines, particularly those from Bubbler and Blanche Cup Spring, are significantly higher than  $^{87}\text{Sr}/^{86}\text{Sr}$  of artesian bores and their reservoir rocks in the Eromanga Basin (Collerson et al., 1988; Uysal, unpublished data). None of the aquifer rocks analyzed previously (Collerson et al., 1988; Ullman and Collerson, 1994) have Sr isotope values high enough to account for the significantly radiogenic Sr isotopic composition of waters from which NFZ-related travertines precipitated. This indicates deep (>3 km) circulation of the groundwater interacting with Neoproterozoic/Cambrian basement and mixing with mantle gas. This is also consistent with high radiogenic  $^4\text{He}$  input into the gas phase, and  $^{234}\text{U}/^{238}\text{U}$  activity ratios of the travertine samples being significantly higher than the equilibrium value of unity (Table 1). Notably, current spring waters along the NFZ have  $^{234}\text{U}/^{238}\text{U}$  activity ratios close to unity (0.9–1.7; Prescott and Habermehl, 2008). Therefore, the substantial increase in  $^{234}\text{U}/^{238}\text{U}$  activity ratios of the travertine veins suggests an external fluid source for explaining the significant U isotopic fractionation (Suksu et al., 2006) (Fig. 11).

High  $^{234}\text{U}/^{238}\text{U}$  activity ratios in water can result from interaction with U-rich rocks (which are also a source of  $^4\text{He}$  production), which produce a physical  $^{234}\text{U}$  flux resulting from  $\alpha$ -recoil release of  $^{234}\text{Th}$  at the water–rock interface (Kigoshi, 1971). Additionally, U isotopes can enter circulating groundwater through chemical processes.  $^{234}\text{U}$  release is controlled by redox conditions in oxidizing environments, in which isotope fractionation is suppressed when  $\text{U}^{6+}$  is present in the form of uranyl carbonate complexes, while under reducing conditions,  $\text{U}^{4+}$  is precipitated as hydroxide or ad-

sorbed onto rock particles (Porcelli, 2008). Therefore, in reducing conditions dissolution and flux of U is reduced and flowing water tends to be enriched in mobile  $^{234}\text{U}$ . In Fig. 11a, samples from Blanche Cup and Bubbler Spring show increasing  $^{234}\text{U}/^{238}\text{U}$  activity ratios as U content decreases. This confirms that the precipitation of these samples was largely controlled by redox conditions with an increased involvement of fluids migrating from depths where reducing conditions prevail. In contrast, samples from Strangways Spring show a positive correlation between  $^{234}\text{U}/^{238}\text{U}$  activity ratios and U content (Fig. 11b), indicating that higher  $^{234}\text{U}/^{238}\text{U}$  activity ratios results from increasing U concentration in more oxidizing fluids contributing a physical  $^{234}\text{U}$  flux through  $\alpha$ -recoil. However, the fluid from which Bubbler and Blanche Cup Spring samples precipitated is much more enriched in U content (Table 1), which is in agreement with higher  $^{87}\text{Sr}/^{86}\text{Sr}$  ratios in samples from Bubbler and Blanche Cup Spring (Fig. 11c). This indicates an increased contribution of deep fluids interacting with U and  $^{87}\text{Rb}$ -rich basement rocks.

### 7.3. Summary

Flux of mantle-derived  $^3\text{He}$  in  $\text{CO}_2$ -rich fluids occurs in deep-reaching fault segments along the NFZ. The  $\text{CO}_2$ -rich  $^3\text{He}$ -bearing fluids interact with the highly radiogenic basement and Eromanga Basin sediments, which produce a significant amount of  $^4\text{He}$ . The  $^4\text{He}$  locally produced in the crust significantly masks (dilutes) the  $^3\text{He}$  mantle component. Fracture controlled deep circulation of Great Artesian Basin waters through basement rock allows mixing of those waters with  $\text{CO}_2$ -rich  $^3\text{He}$ -bearing mantle fluids.

## 8. Discussion

Despite being old and flat Australia is not stable. We have shown evidence for late Quaternary to Recent fault-controlled

mantle  $^3\text{He}$  and  $\text{CO}_2$  degassing along the NFZ in the Australian craton. The seismically active NFZ dissects the entire crust as a sinistral strike-slip fault system decorated by carbonic springs and associated tectonically controlled travertine deposits. The NW-striking NFZ is in a favorable orientation to the E-W-trending  $\sigma_{\text{Hmax}}$  direction of the recent stress field and thus prone to reactivation. The discharge of  $\text{CO}_2$ -rich fluids in this intra-plate setting occurred through seismicity reactivating pre-existing faults and opening new fracture sets that are filled with travertine. Gold and Soter (1984) showed that earthquakes can be triggered by mantle-derived fluids that utilize networks of fractures and faults to ascend through the crust. Such a hydrologic model has been proposed by Karlstrom et al. (2009) to explain elevated  $^3\text{He}/^4\text{He}$  ratios associated with  $\text{CO}_2$  deposits aligned along faults at the southern edge of the Great Artesian Basin. Similar processes have also been observed in other active, crustal/lithospheric-scale structures (Kennedy et al., 1997; Kulogoski et al., 2005; Famin et al., 2008).

### 8.1. Active tectonics, mantle degassing, fluid flow and travertine deposition

In the absence of active magmatism, active faulting is the only viable process creating permeable pathways in the crust facilitating transport of mantle-derived fluids to the surface (Kulogoski et al., 2005; Kennedy and van Soest, 2007; Güleç et al., 2014). Episodic and localized hydrothermal flow occurs during and immediately after earthquakes, which increase permeability along faults (Sibson, 1990, 2005). Over time, permeability falls and compaction of the fault leads to overpressure and promotes slip (Blanpied et al., 1992; Byerlee, 1993).

The active, repeatedly reactivated NFZ is decorated by late Quaternary to Recent springs and travertine deposits that have a regular spacing. The travertine deposits are intensely fractured and newly formed carbonate deposits show evidence of faulting (Fig. 4b). Due to the high  $\text{CO}_2$  content of the Great Artesian Basin waters travertine deposition is still active. The newly formed fracture systems are filled by travertine, while recent precipitation takes place through mound spring vents forming circular ponds (Fig. 4c). Water outflow through artificial bores results in travertine deposition as soon as the water has reached the surface (Fig. 4d) demonstrating that wherever artesian water finds pathways to the surface it instantaneously precipitates carbonate due to pressure release (Uysal et al., 2011). Therefore, immediately after the formation of the fracture systems travertine precipitation commenced and our U/Th ages provide minimum ages of movement in the NFZ.

The U/Th ages suggest distinct age clusters every  $\sim 3\text{--}5$  ka between 26.4 ka and 1.2 ka (Fig. 6). Marrett (1994) investigated scaling relations of intra-plate earthquake recurrence intervals with fault lengths. Faults with a strike length of 70–100 km (comparable to the NFZ, see below) as the Lone Pine and White Wolf faults in California, USA, have recurrence intervals of 5.0–10.5 ka (Lubetkin and Clark, 1988) and 6.7–14 ka (Marrett, 1994). Despite the fact crustal deformation rates in the vicinity of the faults in California are significantly higher than around the NFZ, it may appear conceivable that the age clusters may represent distinct earthquake cycles along the NFZ.

How did the fluids ascend to the surface? We envisage that fluid transport was channelized as there is evidence that the mantle-derived fluids are focused along the NFZ. In the brittle crust deformation involves fracturing and fault-related fractures controlled the orientation of the travertine veins. Rocks in the brittle crust have substantial strength and can support open fracture networks over kilometer-scale distances. In the ductile crust at  $>\sim 12\text{--}18$  km depth, brittle behavior can occur as well (Etheridge, 1983), especially at high strain rates. Data from several earth-

quakes demonstrated that rupture and brittle deformation occur well below the brittle–ductile transition (Priestley et al., 2008). For the Northridge earthquake in California, the main shock occurred at 17–18 km, and aftershocks extended to  $\sim 25$  km (Ague, 2014).

If the fluid pressure exceeds the sum of the tensile strength of the rock and the least principal stress, then hydrofracturing and associated drops in fluid pressure will occur (Hubbert and Willis, 1957; Yardley, 1986). The maximum tensile strength of most rocks is  $\sim 100$  bars, so even modest fluid overpressures will cause hydrofracturing (Ague, 2014). With time, the permeability created by hydrofracturing events is reduced as cracks are sealed. If permeability reaches low enough levels ( $< \sim 10^{-20} \text{ m}^2$ ), then fluid pressure can build up again and produce another hydrofracturing event (Ague, 2014). Episodes of fracturing and healing preserved in veins (Fig. 4) attest to this cyclic behavior (Ramsay, 1980).

As shown by Ague (2014), structures that focus fluid flow (e.g. veins and shear zones) may transfer significantly greater fluxes of fluid, ranging from  $\sim 10^4 \text{ m}^3/\text{m}^2$  to  $>10^5 \text{ m}^3/\text{m}^2$ . Rock failure caused by hydrofracturing or tectonic stress, will create fractures that increase rock permeability and focus flow, as demonstrated for the NFZ. Crack-seal veins can be present at all levels of the crust and are indicators of episodic mass transfer (Ague, 2014).

### 8.2. Crustal/lithospheric deformation and reactivation

The carbonic spring deposits occur at various relatively short fault segments along the NFZ (Fig. 2). Because the focused  $\text{CO}_2$ -bearing fluids contain a mantle component, the various fault segments are probably interlinked at depths. This is supported by fault-growth models showing that larger faults are the result of the growth and linkage of smaller faults (Walsh and Watterson, 1988; Childs et al., 2009). The mantle fluids and the regular spacing of the travertine deposits demand that the NFZ cuts the entire cratonic crust, which in the region is 30–35 km thick (Kennett et al., 2011) (Fig. 1B). If fault scaling relationships (Cowie and Scholz, 1992) are accepted for multiply reactivated, long-lived, linked faults, then these relationships would suggest a strike length of  $\sim 60\text{--}70$  km and a displacement of  $\sim 5$  km. We envisage that these figures provide useful upper limits to a feasible displacement along the NFZ.

Holford et al. (2011) proposed that active intra-plate deformation in south-central Australia is localized and controlled by the thermal properties of the lithosphere. In fact, the NFZ is located near the boundary of a pronounced thermal anomaly (Fig. 1C). The various data sets shown in Fig. 1 all have different resolutions and therefore it is difficult to match them spatially exactly. However, we note that the NW-striking step in lithospheric thickness mapped by Fishwick et al. (2008), the crustal thickness map of Kennett et al. (2011), the heat flow data and the crustal provinces all show major changes along a NW-striking zone that broadly coincides with the NFZ. Very approximately, the NFZ was reactivated where  $S_{\text{Hmax}}$  swings from an E-W into a NNE direction. We suggest that these coincidences are not fortuitous and that the NFZ marks an important, late Quaternary to Recent discontinuity in the middle of the Australian continent. If this interpretation was accepted, it would follow that the NFZ is associated with the step in lithospheric thickness proposed by Fishwick et al. (2008) and its location might be controlled by this step in the lithosphere.

The spatial correlations shown in Fig. 1 suggest to us that the NFZ localized in an area where major discontinuities and transitions are superimposed on each other. A similar case has recently been described by Siler and Kennedy (2016) from the Great Basin of the western US. As in many intra-plate settings, factors such as pre-existing structural weaknesses and zones of overpressured crust play an important role in the distribution of deformation (Sibson, 1995). Pre-existing zones of mechanical weakness such as

faults and shear zones or compositional boundaries exert a first-order control on the localization of intra-plate deformation (Sykes, 1978). The NFZ is a reactivated structure (Adlam and Kuang, 1988) that formed close to a major compositional boundary, the Tasman Line proposed by Shaw et al. (1996), which is associated with the step in lithospheric thickness (Fishwick et al., 2008). The importance of these pre-existing zones gain support from the numerical model results of Dyksterhuis and Müller (2008), which also stress that rheological contrasts can explain localization of deformation. Holford et al. (2011) believe that while all those mechanical weaknesses may influence the deformation within a region, it is the thermal weakening of the lithosphere that is the primary control on which lithospheric segments are prone to deformation/reactivation. Holford et al. (2011) suggest that the thermal anomaly stems from radioactive decay of basement enriched in heat producing elements. Therefore, the heat anomaly is intimately related to the compositional boundary and the question which factor is primarily controlling the development of the crustal/lithospheric-scale NFZ might become semantic.

Whatever the exact control on the reactivation of the NFZ is, the more important aspect appears to us that a crustal/lithospheric scale fault system developed since the late Quaternary in the central part of the Australian craton. East-central Australia is underlain by an area of high-amplitude asthenospheric shear (Conrad et al., 2011) and  $^3\text{He}$  and  $\text{CO}_2$  leaking from the mantle typically occurs in zones of lithospheric-scale faulting. We speculate that the NW-striking major step in lithospheric thickness (Fishwick et al., 2008) associated with the NFZ localized and triggered edge-driven convection as shown by Davies and Rawlison (2014). Edge-driven convection coupled with northward plate motion can generate a cylindrical flow pattern involving upwelling in the shallow asthenosphere, which may have caused lithospheric cracking that ultimately caused  $^3\text{He}$  leaking.

## 9. Conclusions

We have provided evidence for late Quaternary to Recent movement along the NFZ in south-central Australia by dating 26 fault-related travertine samples between 354 and 1.2 ka. There appears to be a clustering of ages every  $\sim$ 3–5 Ma since  $\sim$ 26 Ma, which may reflect fault recurrence intervals at the NFZ. The geochemical data indicate that the NFZ is tapping the mantle and therefore must cut through the entire crust. Elevated  $R/R_a$  values,  $\text{CO}_2/^3\text{He}$  ratios of gas samples, and  $\delta^{13}\text{C}$  data for the travertine deposits are all consistent with a mantle origin of the fluids from which travertine precipitated. Because the mantle signature of the fluid is preserved, relatively rapid upwelling is needed. Furthermore, the spatial correlation between  $R/R_a$  in springs aligned with the NFZ, as opposed to artesian bores away from the NFZ, all provide consistent evidence that circulating mantle-sourced fluids are focused along the NFZ. The  $\text{CO}_2$ -rich  $^3\text{He}$ -bearing fluids interact with the highly radiogenic basement and Eromanga Basin sediments, which produce a significant amount of  $^4\text{He}$ . The  $^{87}\text{Sr}/^{86}\text{Sr}$  isotope compositions of the travertine veins are consistent with deeply ( $>3$  km) circulating, carbonate-forming Great Artesian Basin groundwater.

The NFZ is a reactivated, long-lived fault in south-central Australia. Our data indicate pronounced neotectonic activity along the NFZ, which was reactivated where a major compositional boundary and a significant heat flow anomaly occurs, and a major step in lithospheric thickness has been mapped. As such, the NFZ is an important active discontinuity in central Australia and may be growing into a crustal/lithospheric-scale structure.

## Acknowledgements

This research was funded by the Queensland Geothermal Energy Centre of Excellence (QGECE). We thank A.D. Nguyen, Wei Zhou and Yuxing Feng for laboratory assistance and technical advice, and Alasdair Skelton for a pre-submission review.

## Appendix A. Supplementary material

Supplementary material related to this article can be found online at <http://dx.doi.org/10.1016/j.epsl.2016.09.017>.

## References

- Adlam, R., Kuang, K.S., 1988. An investigation of structures controlling discharge of spring waters in the south western Great Artesian Basin. *Dept. Mines Energy South Australia report 88/4*, 16 pp.
- Ague, J.J., 2014. Fluid flow in the deep crust. In: Holland, H.D., Turekian, K.K. (Eds.), *Treatise on Geochemistry*, vol. 4, second edition. Elsevier, pp. 203–247.
- Balfour, N.J., Cummins, P.R., Pilia, S., Love, D., 2015. Localization of intraplate deformation through fluid-assisted faulting in the lower-crust: the flinders ranges, South Australia. *Tectonophysics* 655, 97–106.
- Ballantine, C.J., Burgess, R., Marty, B., 2002. Tracing fluid origin, transport and interaction in the crust. In: Porcelli, D., Ballantine, C.J., Wieler, R. (Eds.), *Reviews in Mineralogy and Geochemistry—Noble Gases in Geochemistry and Cosmochemistry*, vol. 47. Mineral. Soc. Am., Washington, D.C., pp. 539–614.
- Bergfeld, D., Evans, W.C., Lowenstern, J.B., Hurwitz, S., 2012. Carbon dioxide and hydrogen sulfide degassing and cryptic thermal input to Brimstone Basin, Yellowstone National Park, Wyoming. *Chem. Geol.* 330–331, 233–243.
- Blanpied, M.L., Lockner, D.A., Byerlee, J.D., 1992. An earthquake mechanism based on rapid sealing of faults. *Nature* 358, 574–576.
- Boreham, C.J., Hope, J.M., Hartung-Kagi, B., 2001. Understanding source, distribution and preservation of Australian natural gas: a geochemical perspective. *J. Austral. Petrol. Expl. Assoc.* 2001, 523–547.
- Braun, J., Gesto, F., Burbidge, D., Cummins, P., Sandiford, M., Gleadow, A., Kohn, B., 2009. Constraints on the current rate of deformation and surface uplift of the Australian continent from a new seismic database. *Aust. J. Earth Sci.* 56, 99–110.
- Byerlee, J.D., 1993. Model for episodic flow of high-pressure water in fault zones before earthquakes. *Geology* 21, 303–306.
- Célerier, J., Sandiford, M., Hansen, D.L., Quigley, M., 2005. Modes of active intraplate deformation, Flinders Ranges, Australia. *Tectonics* 24, TC6006.
- Chacko, T., Mayeda, T.K., Clayton, R.N., Goldsmith, J.R., 1991. Oxygen and carbon isotope fractionations between  $\text{CO}_2$  and calcite. *Geochim. Cosmochim. Acta* 55, 2867–2882.
- Cheng, H., Edwards, R., Hoff, J., Gallup, C., Richards, D., Asmerom, Y., 2000. The half-lives of uranium-234 and thorium-230. *Chem. Geol.* 169, 17–33.
- Childs, C., Manzocchi, T., Walsh, J.J., Bonson, C.G., Nicol, A., Schöpfer, M.P.J., 2009. A geometric model of fault zone and fault rock thickness variations. *J. Struct. Geol.* 31, 117–127.
- Clark, T.R., Zhao, J.-X., Roff, G., Feng, Y.-X., Donec, T.J., Nothdurft, L.D., Pandolfi, J.M., 2014. Discerning the timing and cause of historical mortality events in modern Porites from the Great Barrier Reef. *Geochim. Cosmochim. Acta* 138, 57–80.
- Collerson, K.D., Ullman, W.J., Torgersen, T., 1988. Ground waters with unradiogenic  $^{87}\text{Sr}/^{86}\text{Sr}$  ratios in the Great Artesian Basin, Australia. *Geology* 16, 59–63.
- Collins, W.J., Beams, S.D., White, A.J.R., Chappell, B.W., 1982. Nature and origin of A-type granites with particular reference to southeastern Australia. *Contrib. Mineral. Petrol.* 80, 189–200.
- Conrad, C.P., Bianco, T.A., Smith, E.I., Wessel, P., 2011. Patterns of intra-plate volcanism controlled by asthenospheric shear. *Nat. Geosci.* 4, 317–321.
- Cowie, P.A., Scholz, C.H., 1992. Displacement-length scaling relationship for faults: data synthesis and discussion. *J. Struct. Geol.* 14, 1149–1156.
- Davies, D.R., Rawlison, N., 2014. On the origin of recent intraplate volcanism in Australia. *Geology* 42, 1031–1034.
- DeMets, C., Gordon, R.G., Argus, D.F., 2010. Geologically current plate motions. *Geophys. J. Int.* 181, 1–80.
- Dyksterhuis, S., Müller, R.D., 2008. Cause and evolution of intraplate orogeny in Australia. *Geology* 36, 495–498.
- Etheridge, M.A., 1983. Differential stress magnitudes during regional deformation and metamorphism: upper bound imposed by tensile fracturing. *Geology* 11, 213–234.
- Famin, V., Nakashima, S., Boullier, A.M., Fujimoto, K., Hirono, T., 2008. Earthquakes produce carbon dioxide in crustal faults. *Earth Planet. Sci. Lett.* 265, 487–497.
- Fishwick, S., Heintz, M., Kennett, B.L.N., Reading, A.M., Yoshizawa, K., 2008. Steps in lithospheric thickness within eastern Australia, evidence from surface wave tomography. *Tectonics* 27, TC4009.
- Geological Survey of South Australia, Curdimurka, atlas sheet series SH 53-8, 1992 1:250,000.

- Gold, T., Soter, S., 1984. Fluid ascent through the solid lithosphere and its relation to earthquakes. *Pure Appl. Geophys.* 122, 492–530.
- Güleç, N., Mırtlu, H., Hilton, R.D., 2014. Gas geochemistry of Turkish geothermal fluids: He–CO<sub>2</sub> systematics in relation to active tectonics and volcanism. In: Baba, A., Bundschuh, J., Chandrasekharan, D. (Eds.), *Geothermal Systems and Energy Resources: Turkey and Greece*. In: Series: Sustainable Energy Development. CRC Press, pp. 13–23.
- Heier, K.S., Rhodes, J.M., 1966. Thorium, uranium and potassium concentrations in granites and gneisses of the Rum Jungle complex, Northern Territory, Australia. *Econ. Geol.* 61, 3–12.
- Hillis, R.R., Reynolds, S.D., 2000. The Australian stress map. *J. Geol. Soc. (Lond.)* 157, 915–921.
- Hillis, R.R., Sandiford, M., Reynolds, S.D., Quigley, M.C., 2008. Present-day stress, seismicity and Neogene-to-Recent tectonics of Australia's 'passive' margins: intraplate deformation controlled by plate boundary forces. In: Johnson, H., Doré, A.G., Gatliff, R.W., Holdsworth, R., Lundin, E.R., Ritchie, J.D. (Eds.), *The Nature and Origin of Compression in Passive Margins*. In: *Geol. Soc. (Lond.) Spec. Publ.*, vol. 306, pp. 71–90.
- Hilton, D.R., 1996. The helium and carbon isotope systematics of a continental geothermal system: results from monitoring studies at Long Valley caldera (California, U.S.A.). *Chem. Geol.* 127, 269–295.
- Holford, S.P., Hillis, P.R., Hand, M., Sandiford, M., 2011. Thermal weakening localizes intraplate deformation along the southern Australian continental margin. *Earth Planet. Sci. Lett.* 305, 207–214.
- Holocher, J., Peeters, F., et al., 2002. Experimental investigations on the formation of excess air in quasi-saturated porous media. *Geochim. Cosmochim. Acta* 66, 4103–4117.
- Hubbert, M.K., Willis, D.G., 1957. Mechanics of hydraulic fracturing. *Trans. Am. Inst. Min. Metall. Pet. Eng. Inc.* 210, 153–168.
- Italiano, F., Bonfanti, P., Ditta, M., Petrini, R., Slepko, F., 2009. Helium and carbon isotopes in the dissolved gases of Friuli region (NE Italy): geochemical evidence of CO<sub>2</sub> production and degassing over a seismically active area. *Chem. Geol.* 266, 76–85.
- Italiano, F., Yuce, G., Uysal, I.T., Gasparon, M., Morelli, G., 2014. Insights into mantle-type volatiles contribution from dissolved gases in artesian waters of the Great Artesian Basin, Australia. *Chem. Geol.* 378/379, 75–88.
- Jenkins, R.J.F., 1990. The Adelaide Fold Belt: tectonic reappraisal. *Spec. Publ., Geol. Soc. Aust.* 16, 395–420.
- Kampman, N., et al., 2012. Pulses of carbon dioxide emissions from intracrustal faults following climatic warming. *Nat. Geosci.* 5, 352–358.
- Karlstrom, K.E., Love, A., Crossey, L.J., Priestley, S., Asmerom, Y., Embid, E., 2009. Mantle degassing and travertine deposits as neotectonic indicators in the Great Artesian Basin of Australia. *Abstr. Program – Geol. Soc. Am.* 41 (7), 447.
- Kennedy, B.M., Kharaka, Y.K., Evans, W.C., Ellwood, A., Depaolo, D.J., Thordsen, J., Ambats, G., Mariner, R.H., 1997. Mantle fluids in the San Andreas fault system, California. *Science* 278, 1278–1281.
- Kennedy, B.M., van Soest, M.C., 2007. Flow of mantle fluids through the ductile lower crust: helium isotope trends. *Science* 318, 1433–1436.
- Kennett, B.L.N., Salmon, M., Saygin, L., AusMoho Working Group, 2011. AusMoho: the variation of Moho depth in Australia. *Geophys. J. Int.* 187, 946–958.
- Keppel, M., Karlstrom, K.E., Love, A.J., Priestley, S., Wohling, D., DeRitter, S., 2013. Hydrogeological Framework of the Western Great Artesian Basin. National Water Commission, Canberra, ISBN 978-1-922136-06-0.
- Kigoshi, K., 1971. Alpha-recoil <sup>234</sup>Th: dissolution into water and the <sup>234</sup>U/<sup>238</sup>U disequilibrium in nature. *Science* 173, 47–48.
- Krieg, G.W., Rodgers, P.A., Callen, R.A., Freeman, P.J., Alley, N.F., Forbes, B.G., 1991. Curdimurka, South Australia 1:250 000 Geological Map SH 53–8 Explanatory Notes. Geological Survey of South Australia, Adelaide.
- Kulogloski, J.T., Hilton, D.R., Izbicki, J.A., 2003. Helium isotopes studies in Mojave Desert, California: implications for ground-water chronology and regional seismicity. *Chem. Geol.* 202, 95–113.
- Kulogloski, J.T., Hilton, D.R., Izbicki, J.A., 2005. Source and movement of helium in the eastern Morongo groundwater basin: the influence of regional tectonics on crustal and mantle helium fluxes. *Geochim. Cosmochim. Acta* 69, 3857–3872.
- Love, A.J., Shand, P., Karlstrom, K.E., Crossey, L.J., Rousseau-Gueutin, P., Priestley, S., 2013. Geochemistry and travertine dating provide new insights into the hydrogeology of the Great Artesian Basin, South Australia. *Proc. Earth Planet. Sci.* 7, 521–524.
- Lubetkin, L.K.C., Clark, M.M., 1988. Late Quaternary activity along the Lone Pine fault, eastern California. *Geol. Soc. Am. Bull.* 100, 755–766.
- Ludwig, K.R., 2012. User's Manual for Isoplot/Ex: a Geochronological Toolkit for Microsoft Excel, 70 pp.
- Mardia, K.V., 1972. Statistics of Directional Data. Academic Press, London.
- Marrett, R., 1994. Scaling of intraplate earthquake recurrence interval with fault length and implications for seismic hazard assessment. *Geophys. Res. Lett.* 21, 2637–2640.
- Marrett, R., Allmendinger, R.W., 1990. Kinematic analysis of fault-slip data. *J. Struct. Geol.* 12, 973–986.
- Marty, B., Jambon, A., 1987. C<sup>3</sup>He in volatile fluxes from the solid Earth: implications for carbon geodynamics. *Earth Planet. Sci. Lett.* 83, 16–26.
- Neumann, N., Sandiford, M., Foden, J., 2000. Regional geochemistry and continental heat flow: implications for the origin of the South Australian heat flow anomaly. *Earth Planet. Sci. Lett.* 183, 107–120.
- Nuriel, P., Rosenbaum, G., Uysal, I.T., Zhao, J.-X., Golding, S.D., Weinberger, R., Karabacak, V., Avni, Y., 2011. Formation of fault-related calcite precipitates and their implications for dating fault activity in the East Anatolian and Dead Sea fault zones. In: *Geology of the Earthquake Source: A Volume in Honour of Rick Sibson*. In: Geological Society of London, Special Publication, vol. 359, pp. 229–248.
- O'Neil, J.R., Clayton, R.N., Mayeda, T.K., 1969. Oxygen isotope fractionation in divalent metal carbonates. *J. Chem. Phys.* 51, 5547–5558.
- Paul, E., Flöttmann, T., Sandiford, M., 1999. Structural geometry and controls on basement-involved deformation in the northern Flinders Ranges, Adelaide Fold Belt, South Australia. *Aust. J. Earth Sci.* 46, 343–354.
- Petit, J.-P., 1987. Criteria for the sense of movement on fault surfaces in brittle rocks. *J. Struct. Geol.* 9, 597–608.
- Porcelli, D., 2008. Investigating groundwater processes using U- and Th-series nuclides. *Radioact. Environ.* 13, 105–153.
- Prescott, J.R., Habermehl, T.R., 2008. Luminescence dating of spring mound deposits in the southwestern Great Artesian Basin, northern South Australia. *Aust. J. Earth Sci.* 55, 167–181.
- Priestley, K., Jackson, J., McKenzie, D., 2008. Lithospheric structure and deep earthquakes beneath India, the Himalaya, and southern Tibet. *Geophys. J. Int.* 172, 345–362.
- Ramsay, J.G., 1980. The crack-seal mechanism of rock deformation. *Nature* 284, 135–139.
- Reynolds, S.D., Coblenz, D.D., Hillis, R.R., 2002. Tectonic forces controlling the regional intraplate stress field in continental Australia: results from new finite element modeling. *J. Geophys. Res.* 107, 2131–2143. <http://dx.doi.org/10.1029/2001JB000408>.
- Ring, U., 2008. The tectonic evolution of the Franciscan subduction complex: implications for the exhumation of high-pressure rocks in subduction-related accretionary wedges. *Spec. Pap., Geol. Soc. Am.* 445.
- Ring, U., Gerdes, A., 2016. Kinematics of the Alpenrhein–Bodensee graben system in the Central Alps: Oligocene/Miocene transtension due to formation of the Western Alps arc. *Tectonics* 35. <http://dx.doi.org/10.1002/2015TC004085>.
- Sandiford, M., Quigley, M., 2009. TOPO-OZ: insights into the various modes of intraplate deformation in the Australian continent. *Tectonophysics* 474, 405–416.
- Sandiford, M., Wallace, M., Coblenz, D., 2004. Origin of the in situ stress field in southeastern Australia. *Basin Res.* 16, 325–338.
- Shaw, R.D., Wellman, P., Gunn, P.J., Whitaker, A.J., Tarlowski, C., Morse, M.P., 1996. Guide to using the Australian crustal elements map. Australian Geological Survey Organisation Record 1996/30.
- Sibson, R.H., 1990. Conditions for fault-valve behavior. *Geol. Soc. (Lond.) Spec. Publ.* 54, 15–28.
- Sibson, R.H., 1995. Selective fault reactivation during basin inversion: potential for fluid redistribution through fault-valve action. In: Buchanan, J.G., Buchanan, P.G. (Eds.), *Basin Inversion: Geological Society Special Publication*, vol. 88, pp. 3–21.
- Sibson, R.H., 2005. Frictional mechanics of seismogenic thrust systems in the upper continental crust – implications for fluid overpressures and redistribution. *AAPG Mem.* 82, 1–17.
- Siler, D.L., Kennedy, B.M., 2016. Regional crustal-scale structures as conduits for deep geothermal upflow. *Geothermics* 59, 27–37.
- Suksi, J., Rasilainen, K., Marcos, N., 2006. In: Broder, J., Merkel, A., Hasche-Berger, K. (Eds.), *Uranium in the Environment*. Springer, Berlin, Heidelberg, pp. 683–690.
- Sykes, L.R., 1978. Intraplate seismicity, reactivation of pre-existing zones of weakness, alkaline magmatism and other tectonism post-dating continental fragmentation. *Rev. Geophys.* 16, 621–688.
- Teng, F.-Z., Rudnick, R.L., McDonough, W.F., Wu, F.-Y., 2009. Lithium isotopic systematics of A-type granites and their mafic enclaves: further constraints on the Li isotopic composition of the continental crust. *Chem. Geol.* 262, 415–424.
- Torgersen, T., Clarke, W.B., 1985. Helium accumulation in groundwater, I: an evaluation of sources and the continental flux of crustal <sup>4</sup>He in the Great Artesian Basin, Australia. *Geochim. Cosmochim. Acta* 49, 1211–1218.
- Ullman, W.J., Collerson, K.D., 1994. The Sr-isotope record of late quaternary hydrologic changes around Lake Frome, South Australia. *Aust. J. Earth Sci.* 41, 37–45.
- Ünal-Imer, E., Uysal, I.T., Zhao, J.-X., Isik, V., Shulmeister, J., Imer, A., Feng, Y., 2016. CO<sub>2</sub> outburst cycles in relation to seismicity: constraints from microscale geochronology and geochemistry of late Quaternary vein carbonates, SW Turkey. *Geochim. Cosmochim. Acta* 187, 21–40.
- Uysal, I.T., Feng, Y., Zhao, J.-X., Altunel, E., Weatherley, D., Karabacak, V., Cengiz, O., Golding, S.D., Collerson, K.D., 2007. U-series dating and geochemical tracing of late Quaternary travertine in co-seismic fissures. *Earth Planet. Sci. Lett.* 257, 450–462.
- Uysal, I.T., et al., 2011. Seismic cycles recorded in late Quaternary calcite veins:

- geochronological, geochemical and microstructural evidence. *Earth Planet. Sci. Lett.* 303, 84–96.
- Waclawik, V.G., Lang, S.C., Krapf, C.B.E., 2008. Fluvial response to tectonic activity in an intra-continental dryland setting: the Neales River, Lake Eyre, Central Australia. *Geomorphology* 102, 179–188.
- Walsh, J.J., Watterson, J., 1988. Analysis of the relationship between displacements and dimensions of faults. *J. Struct. Geol.* 10, 239–247.
- Weiss, R.F., 1974. Carbon dioxide in water and seawater: the solubility of a non-ideal gas. *Mar. Chem.* 2, 203–215.
- Yardley, B.W.D., 1986. Fluid migration and veining in the Connemara Schists, Ireland. In: Walther, J.V., Wood, B.J. (Eds.), *Fluid–Rock Interactions During Metamorphism*. Springer-Verlag, New York, pp. 109–131.
- Zhao, J-X., Hu, K., Collerson, K.D., Xu, H., 2001. Thermal ionization mass spectrometry U-series dating of a hominid site near Nanjing, China. *Geology* 29, 27–30.